

AD-A156 151

OPTICAL SYNTHETIC APERTURE TECHNIQUES

Final Report

Carl C. Aleksoff

May 1985

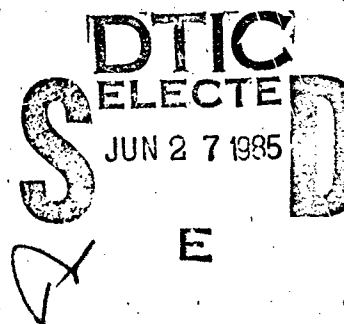
Reproduced From
Best Available Copy

U.S. Army Research Office
P.O. Box 12211
Research Triangle Park, NC 27709
Contract Number: DAAG29-80-K-0008

Environmental Research Institute of Michigan
Infrared and Optics Division
P.O. Box 8618
Ann Arbor, Michigan 48107

DTIC FILE COPY

APPROVED FOR PUBLIC RELEASE;
DISTRIBUTION UNLIMITED.



20000811023

85 06 12 004

THE VIEW, OPINIONS, AND/OR FINDINGS CONTAINED IN THIS REPORT ARE
THOSE OF THE AUTHOR(S) AND SHOULD NOT BE CONSTRUED AS AN OFFICIAL
DEPARTMENT OF THE ARMY POSITION, POLICY, OR DECISION, UNLESS SO
DESIGNATED BY OTHER DOCUMENTATION.

UNCLASSIFIED

SECURITY CLASSIFICATION OF THIS PAGE (When Data Entered)

REPORT DOCUMENTATION PAGE		READ INSTRUCTIONS BEFORE COMPLETING FORM
1. REPORT NUMBER	2. GOVT ACCESSION NO. N/A	3. RECIPIENT'S CATALOG NUMBER N/A
4. TITLE (and Subtitle) Optical Synthetic Aperture Techniques ERIM -		5. TYPE OF REPORT & PERIOD COVERED Final Report 8/1/85-4/30/85
7. AUTHOR(s) C.C. Aleksoff		6. PERFORMING ORG. REPORT NUMBER 151200-17-F
9. PERFORMING ORGANIZATION NAME AND ADDRESS Environmental Research Institute of Michigan P.O. Box 8618 Ann Arbor, MI 48107		8. CONTRACT OR GRANT NUMBER(s) DAA629-80-K-0008
11. CONTROLLING OFFICE NAME AND ADDRESS U. S. Army Research Office Post Office Box 12211 Research Triangle Park, NC 27709		10. PROGRAM ELEMENT, PROJECT, TASK AREA & WORK UNIT NUMBERS
14. MONITORING AGENCY NAME & ADDRESS (if different from Controlling Office) N/A		12. REPORT DATE May 1985
		13. NUMBER OF PAGES 53
		15. SECURITY CLASS. (of this report) Unclassified
		15a. DECLASSIFICATION/CONTROLLING GRADING SCHEDULE
16. DISTRIBUTION STATEMENT (of this Report) Approved for public release; distribution unlimited.		
17. DISTRIBUTION STATEMENT (of the abstract entered in Block 20, if different from Report) NA		
18. SUPPLEMENTARY NOTES The view, opinions, and/or findings contained in this report are those of the author(s) and should not be construed as an official Department of the Army position, policy, or decision, unless so designated by other documentation.		
19. KEY WORDS (Continue on reverse side if necessary and identify by block number) Synthetic Aperture Imaging, Mode-Locked Lasers, Bandwidth Compression Lasers, LIDAR, LADAR, Light, Imaging, Optics, Optical Spectrum Analyzer, Optical Processing.		
20. ABSTRACT (Continue on reverse side if necessary and identify by block number) Optical synthetic aperture imaging concepts and techniques were theoretically and experimentally investigated. The theory of optical synthetic aperture imaging was extended to arbitrary geometries and to multiple sources/receivers. Scanned synthetic aperture imaging was demonstrated at a wavelength of 1.22 mm. A bandwidth compression technique was analyzed and demonstrated that gave fine range resolution with only a narrow passband receiver using mode-locked lasers. A coherent optical spectrum analyzer that uses a tapped optical fiber was conceived and experimentally demonstrated. (over)		

DD FORM 1 JAN 73 1473

EDITION OF 1 NOV 65 IS OBSOLETE

UNCLASSIFIED

SECURITY CLASSIFICATION OF THIS PAGE (When Data Entered)

UNCLASSIFIED

SECURITY CLASSIFICATION OF THIS PAGE(When Data Entered)

ABSTRACT (Cont.) Block 20

Special backprojection concepts were conceived that can process certain types of synthetic aperture data. Grating interferometer processing techniques were also investigated. (A)

UNCLASSIFIED

SECURITY CLASSIFICATION OF THIS PAGE(When Data Entered)

OPTICAL SYNTHETIC APERTURE TECHNIQUES

CONTENTS

Introduction.....	1
Summary of Results.....	2
Conclusion.....	3
Appendix A: Synthetic-Aperture Techniques at Near-Millimeter Wavelengths.....	5
Appendix B: Generalized Imaging.....	16
Appendix C: Laser Heterodyne Ranging Using a Mode-Locked Local-Oscillator for Bandwidth Compression.....	23
Appendix D: Tapped-Fiber Spectrum Analyzer.....	33
Appendix E: Optical-Hybrid Backprojection Processing.....	34
Appendix F: Grating-Based Interferometric Processor for Real-Time Optical Fourier Transformation.....	42
Appendix G: Additional Requested Information.....	53

Accession For	
NTIS GRA&I	<input checked="" type="checkbox"/>
DTIC TAB	<input type="checkbox"/>
Unannounced	<input type="checkbox"/>
Justification	
By _____	
Distribution/	
Availability Codes	
Dist	Avail and/or Special
A-1	



OPTICAL SYNTHETIC APERTURE TECHNIQUES

INTRODUCTION

The goal of this program is to develop optical synthetic aperture (OSA) imaging concepts and techniques.

Active synthetic aperture radar systems have been used at microwave wavelengths for many years to produce quality imagery. Directly emulating such systems at optical wavelengths is not adequate. As the wavelength of the transmitted/received radiation decreases, a wavelength is reached typically in the near millimeter wavelength region, where the received signal can no longer be directly detected and classically demodulated to obtain the required phase information. Rather, it becomes necessary to use heterodyne and/or interferometric techniques in order to obtain the phase information. Further, at least presently, optical sources, such as lasers, cannot be waveform controlled in the same manner as microwave sources. Thus, different concepts, techniques, and hardware implementations are required for OSA imaging.

During this program, a number of different aspects of OSA imaging systems have been investigated as described in the next section and appendices. They include a generalization of the theory describing SAL imaging, a new transmitter/receiver configuration, a new optical spectrum analyzer for OSA systems and other applications, and the development of a specific hybrid processing configuration for processing OSA data.

SUMMARY OF RESULTS

The theory for generating OSA imagery was extended in its generality to include arbitrary positions of the source(s) and receiver(s) for active systems and includes arbitrary receiver positions for passive systems. In general, given arbitrary object size and motion, the required processing is space variant. However, with certain geometry and object size limitations, the processing becomes space invariant. Far field conditions lead to being able to efficiently process the data via Fourier transform algorithms. One such case was experimentally demonstrated at a wavelength of 1.22 mm. This was the first SAL image produced at near millimeter wavelengths. See Appendix A.

Some analysis was also done regarding "generalized imaging" of which OSA imaging is a subset. See Appendix B.

Wide bandwidth transmitted signals are required for high resolution range-doppler SAL imaging. Mode-locked lasers easily produce wide bandwidth output but the efficient detection and processing of such signals can be troublesome. A technique was developed to reduce the required detection (receiver) bandwidth without losing the high resolution imaging capability. It consisted of not only a mode-locked transmitter laser but also of a mode-locked local oscillator laser in a heterodyne detection setup that allowed the received signal to be compressed into a narrow bandwidth. A bandwidth reduction of over 500 was experimentally demonstrated. See Appendix C.

A useful instrument for obtaining the modulation information from a wide bandwidth optical OSA signal would be a high finesse optical spectrum analyzer that spatially displays the temporal spectrum with a one-to-one linear correspondence between the temporal frequency and the

spatial position. Such an output would allow direct optical processing or detection with a linear detector array for digital processing without requiring correction for a non-linear correspondence. Towards the objective, a spectrum analyzer was conceived and demonstrated that was composed of a multi-tapped optical fiber delay line in conjunction with a holographic matched filter. This combination produces the desired linear spatial distribution of the temporal spectrum of the light fed into the optical fiber. See Appendix D.

The processing of the three dimensional signal history data is, of course, an essential aspect of OSA imaging. In general, the processing can be very computationally burdensome. However, by properly picking the geometry and signal modulation, the data takes on a form that is conveniently processed using backprojection techniques similar to that used with tomographic imaging systems. In particular, a hybrid (optical-digital) processor concept that allowed such data to be efficiently processed was initially conceived under this contract and then was experimentally demonstrated with other support. The further development of such a processor has the potential to lead to a real-time processor of OSA imagery. See Appendix E. Also, the grating interferometer type of processor appears attractive for a similar type of OSA processing. The advantage of the grating interferometer lies in its achromatic characteristics which considerably reduce the requirements on the source coherence. See Appendix F.

CONCLUSION

The concepts, analysis, and experimental results developed in this program have helped establish the feasibility of optical synthetic aperture imaging and hopefully has laid the foundation for an operational optical synthetic aperture system.

APPENDIX A

SYNTHETIC-APERTURE TECHNIQUES AT NEAR-MILLIMETER WAVELENGTHS*

Carl C. Aleksoff

Abstract

Synthetic aperture (SA) imaging techniques are considered for identifying targets at ranges of a few kilometers using near-millimeter waves. A generalized concept of SA imaging is presented. A hybrid SA array technique is proposed that would significantly diminish the motion required for the SA data generation. A scanning SA technique is presented and analyzed in detail. Images are shown that were generated using the scanning SA technique with a near-millimeter wave homodyne system operating at 1.22 mm.

*This paper was presented at the Millimeter Optic Session of the SPIE's Huntsville Electro-Optical Technical Symposium, October 1-2, 1980. It was published in the Proc. SPIE, Vol. 259, Millimeter Optics, 1980, pp 115-124.

Synthetic-aperture techniques at near-millimeter wavelengths

Carl C. Aleksoff

Radar and Optics Division, Environmental Research Institute of Michigan
P.O. Box 8618, Ann Arbor, Michigan 48107

Abstract

Synthetic aperture (SA) imaging techniques are considered for identifying targets at ranges of a few kilometers using near-millimeter waves. A generalized concept of SA imaging is presented. A hybrid SA array technique is proposed that would significantly diminish the motion required for the SA data generation. A scanning SA technique is presented and analyzed in detail. Images are shown that were generated using the scanning SA technique with a near-millimeter wave, homodyne system operating at 1.22 mm.

Introduction

Some previous publications have indicated that near-millimeter (NMM) wave systems might be applicable for imaging through fog, smoke, or rain in battlefield situations where visible or infrared wavelength imaging systems are blinded.¹⁻³ The goal is that the NMM wave imaging system would be of a small enough size that it can be conveniently mounted on a vehicle and still have a large enough aperture to enable recognition of tactical targets at ranges up to several kilometers. According to Kruse¹, recognition of tactical vehicles requires about a 0.5 m resolution capability.

The required aperture width w_1 (Rayleigh criteria) of a classical one-dimensional imaging system to achieve a resolution of p at a range R with wavelength λ is given by

$$w_1 = \frac{\lambda R}{p} \quad (1)$$

or if the system is a focused scanning type that uses a common aperture to both transmit and receive the signal, then the aperture width is given by half of Eq. (1) or

$$w_2 = \frac{\lambda R}{2p} \quad (2)$$

Typically, the NMM wavelengths are taken to run from 0.3 mm to 3 mm. Figure 1 shows the aperture widths required for a 0.5 m resolution as a function of range for 0.3 mm, 1.22 mm, and 3 mm wavelengths as described by the more optimistic Eq. (2). It is clear from Figure 1 that operation of a scanning system at a wavelength of 0.3 mm and up to 3 km ranges would require an aperture of about 1 m, which is about the maximum size classical antenna (dish) that would be tolerated. However, atmospheric attenuation considerations tend to drive the operating wavelength selection to longer wavelengths³. Operation at the other end of the NMM wave region, i.e., 3.0 mm wavelengths, leads to a 10 m aperture requirement, which obviously implies an impractically sized classical antenna for mounting on a vehicle, especially in battlefield situations. Thus, one is led to considering alternative techniques such as synthetic aperture imaging systems.

Synthetic aperture techniques

By synthetic aperture (SA) imaging, we imply that a series of steps of the type illustrated in Figure 2 are used to produce the imagery. We start with an object (in object space) illuminated with a specific wavefront. The signal scattered by the object depends on the geometrical positions of the transmitters, detectors, and object as well as specific scattering characteristics of the object and the spectral properties of the illumination. The SA technique is dependent on setting up the object space such that the scattered signal has temporal variations due to changing parameters in object space, which could be caused by

1. Temporal modulations in the transmitted signal (e.g., chirping or pulsing).
2. Transmitter and/or detector motion (including switching between sources and/or detectors in arrays).
3. Object motion (e.g., a rotating object).
4. Beam scanning (e.g., scanning a transmitted wavefront with a rotating mirror).

The scattered signal in conjunction with an arbitrary modifying signal gives an electrical signal which we will denote as the SA temporal signal. The modifying signal could be a

local reference wave heterodyned with the scattered signal or some more complicated combination of signals, electrical and electromagnetic. The one-dimensional temporal signal is then distributed into a multi-dimensional spatial space (spatial signal space) via a specific formatting procedure. This spatial signal is what is often referred to as the synthetic aperture data and the extent of the data defines the synthetic aperture. The spatial signal space might also be referred to as a hologram, especially when the signal is recorded onto photographic emulsion. However, the spatial signal could as well be distributed in a computer memory where the spatial coordinates are just conceptual aids for proper data retrieval in the next step. This next, and last step, is processing the spatial signal data to give an image. The processing could be optically implemented Fourier transform or a digitally implemented FFT, holographic processing, or more complicated procedures.

Often two different types of object space parameters can be changed simultaneously to generate the data for two dimensional imaging. For example, the classical side-looking SA radar uses the combination of range information derived by transmitting a temporally modulated waveform and Doppler information derived from the motion of the aircraft.⁴⁻⁶

Such a "side-looking" SA system also appears attractive using NMM waves in battlefield scenarios. However, the actual type of system is more likely dictated by the types of NMM wave sources, detectors, and components available rather than any idealized considerations. If highly coherent (phase stable) sources of adequate power output and efficiency (small size) are available, then heterodyne systems are attractive. If detectors and components (e.g., mixers) are also available, then direct detection and subsequent mixing of the electrical signal could be used, much as for the microwave SA radars. If coherence of the sources is a problem or if atmospheric turbulence is a problem, then interferometric techniques could be used, much as has been demonstrated at optical wavelengths or at radio wavelengths for radio astronomy. The distinction between microwave (thermal noise limited systems) and optical (photon noise limited systems) becomes blurred for NMM waves and a hybrid system will probably be required in order to blend the best of microwave and optical techniques.

Let us consider how various SA techniques might be implemented. Given tactical situations, consistent movement of a target is not likely and hence target motion will not be considered. However, modulation and source/detector motion will be considered.

In a modulated radar system, we know that the range resolution capability is given by

$$\rho_r = \frac{c}{2B} \quad (3)$$

where c is the free space speed of light and B is the transmitted bandwidth. Thus, for a 0.5 m resolution at a 1.2 mm wavelength, a bandwidth of 300 MHz is required, which is only a 0.1% bandwidth to carrier frequency ratio. This bandwidth appears to be easily obtainable as a frequency chirp generated with a backward wave oscillator or as a pulse train generated with a mode locked laser. Thus, ranging appears to be a good candidate for gathering SA data with NMM waves.

As with microwave SA radar systems operated from aircraft, we can also envision the cross-range data being generated via the motion of the vehicle carrying the NMM wave SA system. That is, Doppler or interferometric information is gathered to synthesize the aperture data in a dimension orthogonal to the range direction, thus allowing the generation of a two dimensional image. This can be accomplished as illustrated in Figure 3 for a homodyne (Doppler) type of SA imaging system. A diverging NMM wavefront emanates from a small aperture (antenna or lens) and illuminates the object. The scattered signal is received with the same aperture and heterodyned. For such a system to straightforwardly process the signal, the position of the receiver/transmitter phase center must typically be known to an accuracy on the order of a tenth of the operating wavelength during its coherent integration time. This is known as motion compensation data. Thus, for a 1 mm SA system, the position knowledge must be on the order of 0.1 mm for up to 10 m of travel. This type of accuracy can be obtained if some reference scatterers (e.g., retro-reflectors) are continually addressed during the vehicle motion with an optical or E&M distance measuring system. In fact, it should even be possible to use the NMM wave SA system itself to generate motion compensation signals from reference reflectors that are illuminated at the same time as the target.

Figure 4 illustrates an alternative hybrid SA array technique where a long thinned array (one-dimensional) is used along with physical motion to fill in the gap between antennas. For example, if 9 small antennas were spaced 1 m apart, then the entire array could be moved slowly in a track by 1 m while quickly switching (electronically) the transmission/receiving across the array to obtain a filled 10 meters worth of SA data.

There are other hybrid SA techniques that can be used, but as stated earlier, the most effective technique may end up being more determined by hardware constraints than conceptual constraints.⁷ Experimental efforts are required to determine the effectiveness of the various SA concepts considering the hardware constraints, atmospheric turbulence and scattering effects, and ground clutter problems. In the next section, we will describe a SA experiment that is in a very early stage of demonstrating NMM wave SA imaging capabilities.

Scanned SA imaging

Consider first the classical scanned imaging system illustrated in Figure 5a. A focused beam is scanned past the target using a rotating mirror. The amplitude or intensity of the received signal scattered from the target is displayed on a screen with its position proportional to the scan angle. In Figure 5b, the SA scanned system is schematically illustrated. However, in this system, a diverging wavefront is scanned past the target using the rotating mirror. The received signal (heterodyne detection) is stored in a memory until the entire target is scanned and then the signal is processed to form the image. Both systems have the same resolution limit, namely that given by Eq. (2) where W_2 is the width of the scanning mirror. The SA system usually can have simpler optics since only a diverging beam is needed and it does not have to be focused to a specific range with the optics. However, time must be spent to process the SA data before the image is formed. The SA scanning system has the advantage that it can refocus by reprocessing the data and hence only one scan is necessary, however, it must keep the SA data in memory.

Let us now develop the processing concept for scanned SA imaging (refer to Figure 6). In this figure, S is a point source, D a point detector, P_n is the n th point scatterer of N scatterers making up the target, and M is the scanning mirror. From the vantage position of the source and detector, the object point appears to move in a circle of radius c_n centered at the mirror rotation center. In fact, it would move on a sphere if the mirror were a two-dimensional scanning type, however, for simplicity, we will confine ourselves to only considering a one-dimensional scan. In regards to Figure 1, it is the rotation of the mirror that produces the "change" indicated after the first box. With respect to Figure 6, let the transmitted signal from S be a diverging spherical wave of the form

$$\frac{1}{r} \exp [i\omega t - kr] \quad (4)$$

where, as usual, $k = 2\pi/\lambda = \omega/c$. The signal scattered back to the detector is of the form

$$U'(t) = \sum_n^N \frac{\sigma_n}{r_n \sigma_n} \exp \{ i[\omega t - k(r_n + d_n)] \} \quad (5)$$

where σ_n is the scattering coefficient for the n th scatterer, r_n is the distance from the source to the n th scatterer, and d_n is the distance from the detector to the n th scatterer. After homodyning with the local oscillator $\exp(i\omega t)$, the detected signal is proportional to

$$U(t) = \sum_n^N \sigma_n \cos \left[\frac{2\pi}{\lambda} (r_n + d_n) \right] \quad (6)$$

where σ_n not only accounts for the scattering efficiency, but also losses in the system as well as $(r_n d_n)^{-1}$ which we assume is so slowly changing that it can be taken as a constant. Also, σ_n is assumed to be real for simplicity sake. Of course, r_n and d_n are functions of time since they vary with mirror position. The signal $U(t)$ is the temporal signal referred to in the second box of Figure 1, while the local oscillator is the modifying signal. The next step is to consider the formatting.

Towards understanding the formatting process, we first note from Eq. (6) that the terms in the summation are cyclic in $r_n + d_n$. In fact, $r_n + d_n = q$, $q = 0, 1, 2, \dots$ describe a set of ellipsoids of revolution in space with S and D as foci. We will denote these "imaginary" surfaces as virtual fringes, for a reason to soon become evident. Consider the holographic recording setup illustrated in Figure 7. The hologram is to be recorded on the recording surface using a spherical wavefront converging to D and a diverging wavefront emanating from S. The recording at the point P is given by

$$|A \exp [-i(\omega t - kr)] + B \exp [-i(\omega t + kr)]|^2 \\ = A^2 + B^2 + 2AB \cos [k(r + d)] \quad (7)$$

Notice that the phase term depends on $r + d$ and then compare to Eq. (6). The hologram recording made under these conditions has the same form as the signal received with the SA system. That is, each term in Eq. (6) can be considered to be a hologram recorded on a circle of radius c_n and formed by the interference between a spherical wavefront converging to the detector D and a diverging wavefront emanating from the source S. Thus, the concept of virtual fringes in the SA system are derived from the real fringes of this comparison holographic recording.

Keeping this holographic concept in mind, the signal $U(t)$ is recorded along a circle in recording space by formatting $U(t)$ into the function $U(\rho, \phi)$ via the relationship

$$U(\rho, \phi) = \int U(t) \delta(\rho - \rho_0, \phi - 2\phi_M) dt \quad (8)$$

where (ρ, ϕ) are polar coordinates in recording space, ρ_0 is an arbitrary constant, $\delta(\rho, \phi)$ is a two-dimensional delta function, and ϕ_M is the angular position of the mirror at time t and hence is a function of t . Recall that the object will appear to rotate at twice the angle of the mirror rotation angle. If the mirror rotates at a constant angular rate of Ω , then we can write that $\phi_M = \Omega t$.

The processing step is a holographic type of reconstruction as illustrated in Figure 8. Within the limitations of the Fraunhofer approximation, the image complex amplitude is described by⁸

$$U_I(R, \theta) = \mathcal{F}\{U(\rho, \phi) U_c(\rho, \phi) w(\rho, \phi, R, \theta)\} \quad (9)$$

where $\mathcal{F}\{\cdot\}$ represents a two-dimensional Fourier transform, $U_c(\rho, \phi)$ is the reconstruction wavefront, $w(\rho, \phi, R, \theta)$ is the propagation kernel, and (R, θ) are the polar coordinates in image space. When Eq. (5) is substituted into Eq. (9) we obtain

$$U_I(R, \theta) = \sum_n^N S_n(R, \theta) + S_n^*(R, \theta) \quad (10)$$

where

$$S_n(R, \theta) = \mathcal{F}\left\{U_c \cdot w \cdot \frac{1}{2} \int \exp\left[\frac{2\pi}{\lambda}(r_n + d_n)\right] \delta(\rho - \rho_0, \phi - 2\phi_n) dt\right\} \quad (11)$$

We note that S_n is the spread function corresponding to the object point P_n . The quality of the image can be determined from the characteristics of the spread function. Aberrations, for example, can be analyzed by comparing the position of each spread function to that of its corresponding object scatterer point. Rather than expand and analyze Eq. (11) in detail for arbitrary configurations, we will consider a special case that not only is straightforward and demonstrates the concept, but corresponds to our experimental setup.

As indicated in Figure 9, consider the case where the source and detector are in the same position and the wavefronts collimated. Hence, the virtual fringes have degenerated to equally spaced straight lines of period $\lambda/2$. If the mirror is rotating at constant angular frequency Ω , then the received signal, as described by Eq. (6), becomes

$$U(t) = \sum_n^N \sigma_n \cos\left[\frac{4\pi}{\lambda} c_n \cos(2\Omega t - \theta_n) + \alpha\right] \quad (12)$$

where α is a constant describing the phase delay within the system optics. Note that c_n and θ_n are both constants. The formatting procedure gives the function

$$U(\rho, \phi) = \sum_n^N \sigma_n \cos\left[\frac{4\pi c_n \rho}{\lambda \rho_0} \cos(\phi - \theta_n) + \alpha\right] A(\rho, \phi) \quad (13)$$

where $A(\rho, \phi)$ describes the effective aperture (a section of circular arc)

$$A(\rho, \phi) = \int_0^T \delta(\rho - \rho_0, \phi - \Omega t) dt \quad (14)$$

and T is the scan period. Notice that the n th term in the summation in Eq. (13) describes a sinusoidal grating with amplitude σ_n , frequency $2c_n/\lambda\rho_0$, angular orientation θ_n , and offset a . The processing now degenerates to using $U_c = 1$ and $W = 1$ in Eq. (9) to give

$$U_I(R, \Theta) = a(R, \Theta) * \left\{ 2 \sum_n^N \left[\sigma_n \delta(R - R_n, \Theta - \theta_n) e^{-i\alpha} + \sigma_n \delta(R - R_n, \Theta + \theta_n) e^{i\alpha} \right] \right\} \quad (15)$$

where spread function $a(R, \Theta)$ is the Fourier transform of $A(\rho, \phi)$ and

$$R_n = \frac{c_n}{\lambda\rho_0} \quad (16)$$

Eq. (15) indicates that we get the usual dual images from the holographic process. Since the center of rotation is outside the object and the object would typically subtend less than 180° , then the two images do not overlap. This is the desired imaging result.

Experimental Results

Figure 10 schematically illustrates the scanning NMM wave SA system that was used to generate our experimental data. This system is part of a MICOM NMM wave radar.¹⁰ The source is a $\text{Cl}^{13}\text{H}_3\text{F}$ waveguide laser pumped by a CO_2 laser. The expanded and collimated CW output at 1.22 mm is scanned with a flat 12 inch diameter mirror. Part of the beam is tapped off with a beamsplitter and forms the local oscillator for homodyne operation. The return signal from the target along with the local oscillator signal are detected (homodyned) at a Golay cell which has about a DC to 15 Hz bandwidth.

Figure 11(a) shows a plot of a received signal from a 60 mm diameter corner-reflector that was 117 cm from the rotation center of the scanning mirror. The total scan angle was 17.5° and the signal data was digitized at 350 samples corresponding to 0.05° intervals. The reflector was within the same room as the NMM wave system in order to avoid atmospheric degradations, at least in the initial experiments. Compare the signal in Figure 11(a) to that in Figure 12(a) which is a computer simulated signal from an idealized point scatterer illuminated with infinite width plane waves. The actual return is obviously not "ideal". The non-symmetric effects may be due to polarization effects from the corner-reflector since the reflector was not symmetrically orientated in the scanning direction. Also, feedback effects from the reflector into the laser were evident. Further, the output beam was somewhat Gaussian shaped with a full width at half power points of about 100 mm.

For our computations the discrete version of Eq. (9) was used for unity magnification, namely

$$U_I(R, \Theta) = \sum_{m=1}^M U(R_0^{-1}, m\Delta\phi) \cos\left[\frac{4\pi R}{\lambda} \cos(\Theta - m\Delta\phi)\right]$$

where $R_0 = 1170$ mm and $\Delta\phi = 0.05^\circ$, and $M = 351$. The image shown in Figure 11(b) was obtained by taking a cut through image space along an arc of radius R_0 as described by the image samples

$$I_q = |U_I(R_0, q\Delta\phi)|^2 \quad q = 1, \dots, 351$$

Figure 12(b) is a construction of the image formed from the "ideal" signal. In comparison, the experimental results show the expected narrow spike from the corner reflector but with a high level of background noise. It is expected that some additional processing, such as bandpass filtering the signal, should improve the quality of the image. However, it should be noted that the theoretical resolution of 7 mm at the target for a 100 mm wide Gaussian wavefront was achieved as demonstrated by the experimental results.

Acknowledgments

The help of G. Tanton, G. Grisham and D. Thompson with the MICOM NMM wave radar is gratefully acknowledged. This work was supported by the U.S. Army Research Office.

References

1. Kruse, P.W., "A System Enabling the Army to See Through Inclement Weather," U.S. Army Advisory Panel Report, 1974.
2. Kruse, P.W., Hartman, R.L., Gamble, W.L., and Guenther, B.D., "Submillimeter System for Imaging Through Inclement Weather," The Optical-Submillimeter Atmospheric Conference, Puerto Rico, 1976.
3. Hartman, R.L. and Kruse, P.W., "Quasi-Imaging Near Millimeter Wave Radar," 1978 International Conference on Submillimeter Wave Propagation.
4. Cindrich, I., Marks, J., and Klooster, A., "Coherent Optical Processing of Synthetic Aperture Radar Data," Symposium Proceeding of Optics in Radar Systems, SPIE Proc., Vol. 128, p. 128, 1977.
5. Aleksoff, C.C., "Synthetic Interferometric Imaging Technique for Moving Objects," Applied Optics, 15, p. 1923, 1976.
6. Walker, J.L., "Range-Doppler Imaging of Rotating Objects," IEEE Trans. Aero. & Elect., AES-16, 23, 1980.
7. Miyashita, T., "Novel Imaging with Fine Range Resolution Using Multifrequency Hologram Matrix of Nonuniformly Space Frequency Series," Proc. of the IEEE, 68, p. 1018, 1980.
8. Farhat, N.H., "A New Imaging Principle," Proc. of the IEEE, 66, p. 379, 1978.
9. Goodman, J.W., Introduction to Fourier Optics, McGraw-Hill, 1968.
10. Tanton, G.A., Morgan, R.L. and Otten, W.G., "An Atmospheric Limit on Submillimeter Wave Imaging: Effects of Transmission Fluctuation Averaging," Millimeter Optics SPIE Proc. Vol. 259.

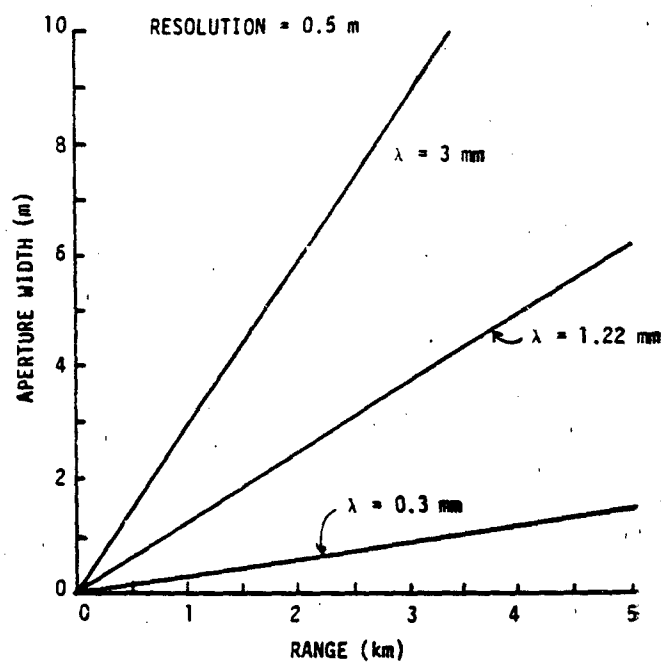


Figure 1. One dimensional aperture width required for 1/2 meter resolution as a function of range.

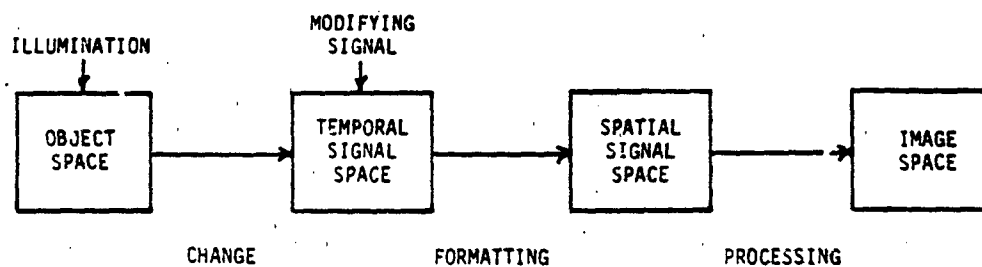


Figure 2. Flow diagram for the synthetic aperture technique.

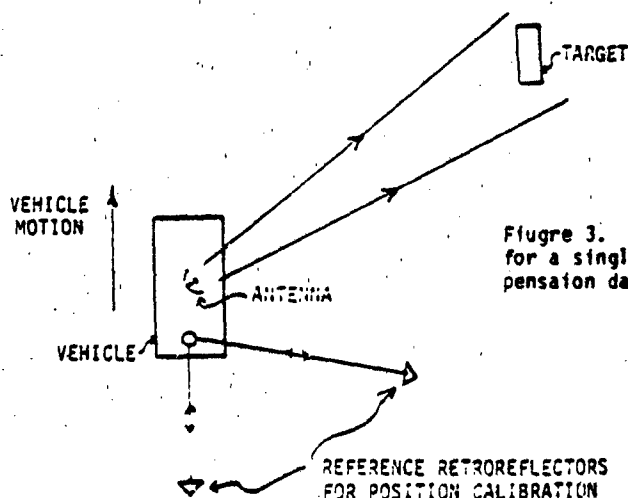


Figure 3. Synthetic aperture image configuration for a single antenna (side-looking). Motion compensation data is derived from the reference retroreflectors.

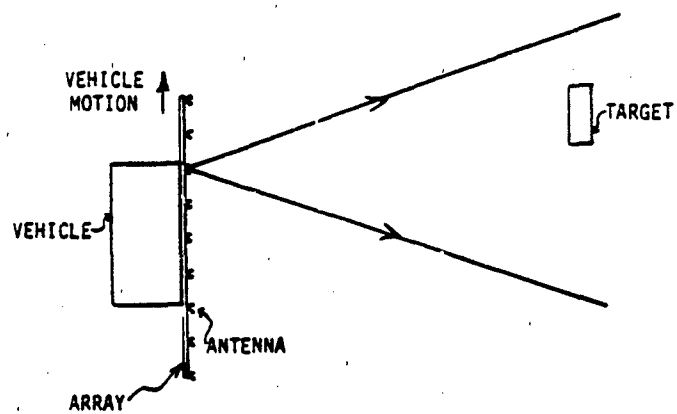


Figure 4. Hybrid synthetic aperture techniques where a thin array is filled-in by translating the array.

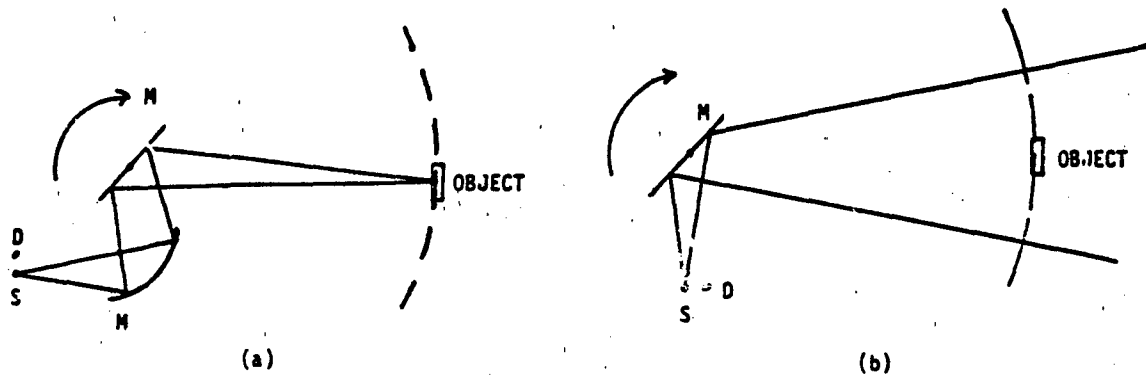


Figure 5. Scanned imaging systems. (a) The classical scanning system. (b) The SA scanning System.

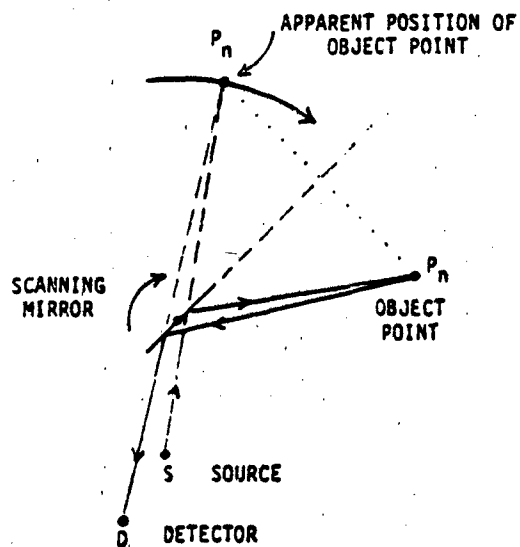


Figure 6. The apparent motion of the object as observed in reflection from the rotating mirror.

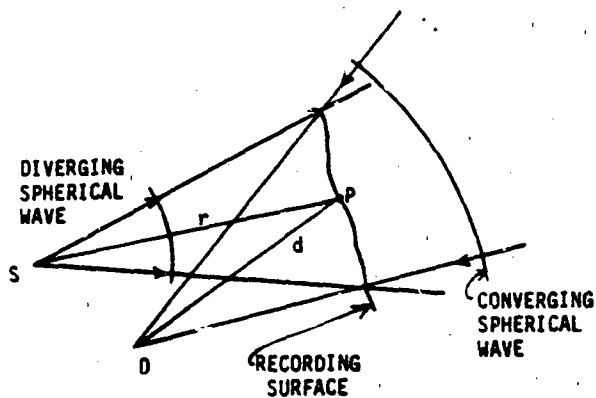


Figure 7. Holographic recording setup.

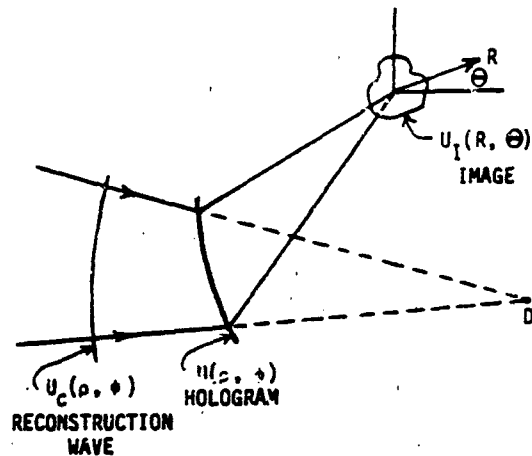


Figure 8. The processing represented as a holographic reconstruction processing.

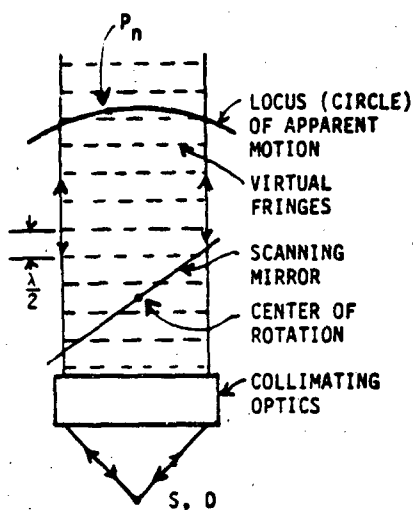
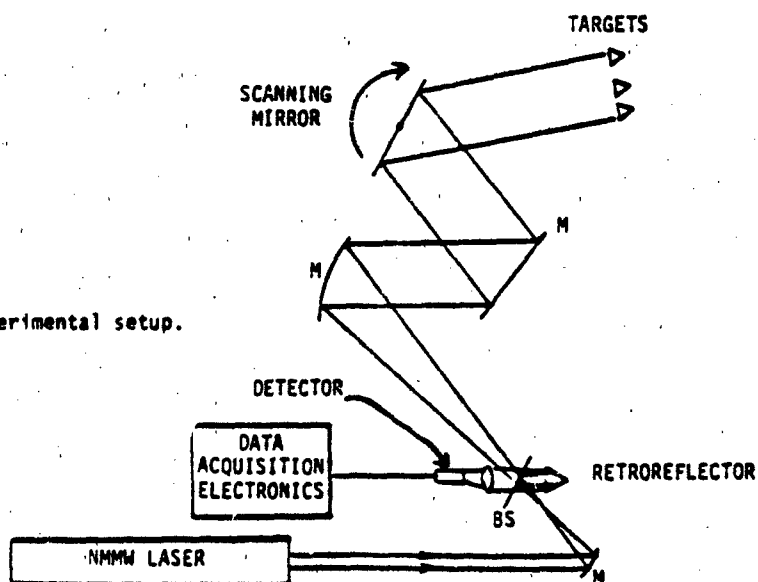


Figure 9. Collimated case with the source and detector coincident.

Figure 10. The experimental setup.



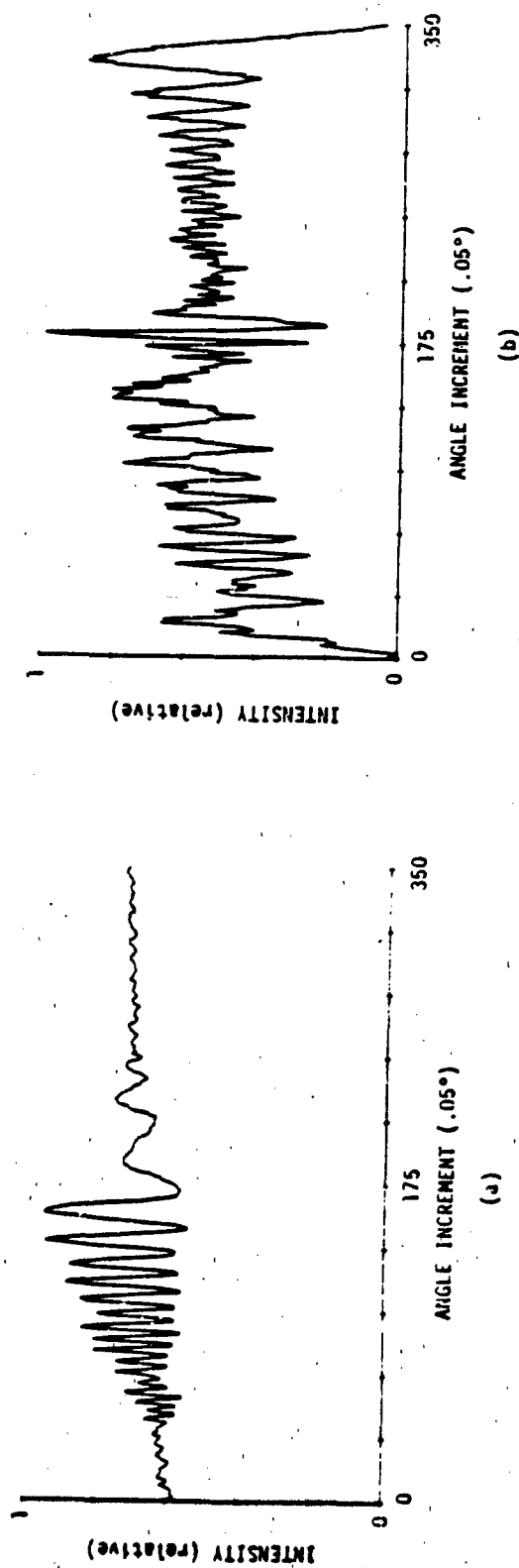


Figure 11. The experimental results for a single corner reflector target. (a) The temporal signal as a function of scan angle. (b) The image along a radius of 117 cm for unity magnification processing.

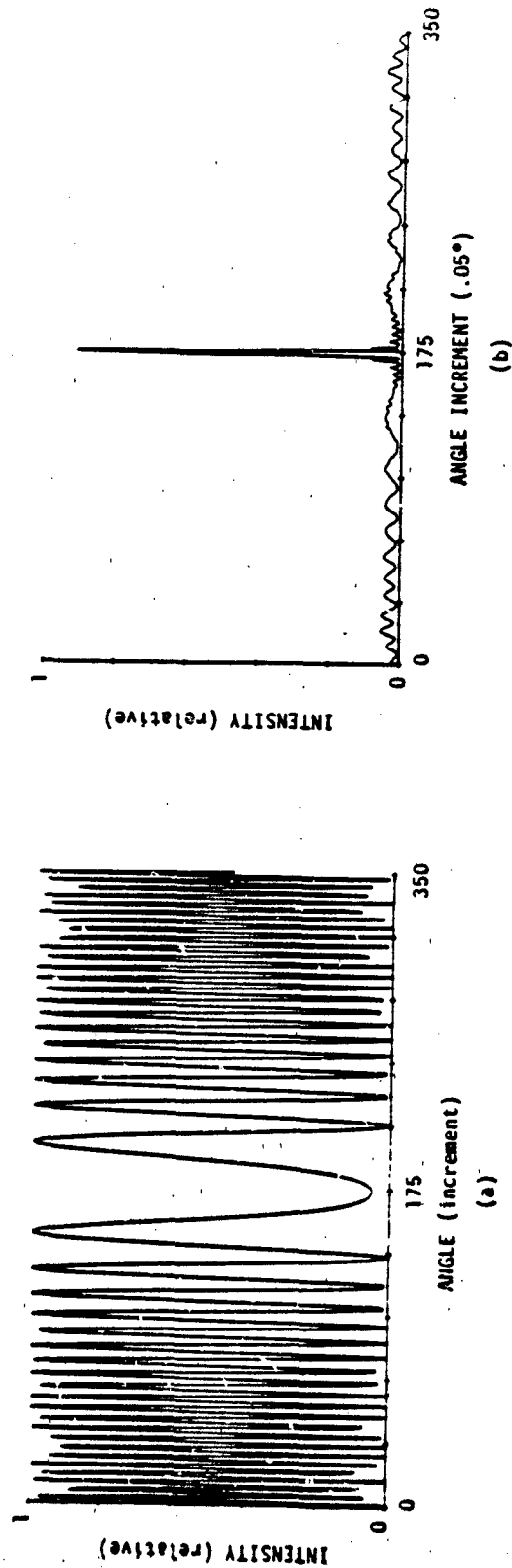


Figure 12. Simulated results for the same parameters as for Figure 11 assuming an ideal point scatterer. (a) The temporal signal. (b) The image.

APPENDIX B

GENERALIZED IMAGING*

Carl C. Aleksoff

Abstract

This paper approaches the questions of what are the fundamental elements of an imaging system and what do we mean by imaging. The whole chain of imaging, from the source of energy to the utilization of the final data is broken into attributes as the basis for further analysis.

*This paper was presented at the "Limits of Passive Imaging Workshop" May 1983 and is published in its proceedings, pp. 21-26. These proceedings can be obtained from C. C. Aleksoff, ERIM, P.O. Box 8618, Ann Arbor, MI 48107.

GENERALIZED IMAGING

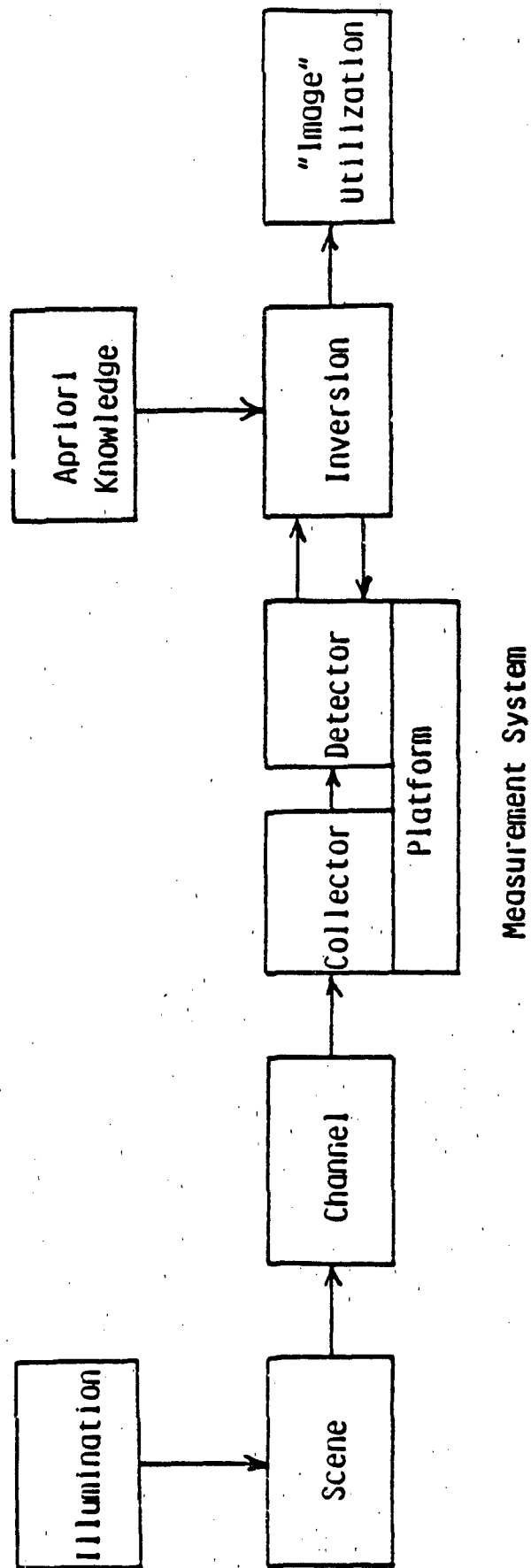
C.C. Aleksoff

The goal of this paper is to start our thinking process about what are the fundamental elements of an imaging system and what do we understand of these elements. The workshop goal is to identify those areas where research is warranted.

The word "imaging" usually brings to mind the human type of visual system consisting of a lens and an array of photoreceptors. Processing is then done on the entire array of photoreceptor outputs. However, it is clear that insects and other creatures have significant variations on this theme. Man made scanning systems and synthetic aperture systems also do not fit in that mold. It appears that in order to properly cover all the possibilities we need to understand the whole chain of imaging, from the source of energy and its properties to the very utilization of the final data. What is it that has not been exploited? It is the much broader class of generalized imaging that we wish to attack.

Imaging can be usefully subdivided for analysis into the set of categories indicated by the boxes in Figure 1. They consist of

1. Illumination (of the scene)
2. Scene
3. Channel (scene to collector interval)



GENERALIZED "IMAGING"

Figure 1

4. Measurement system (which consists of collectors and detectors on platforms)
5. Inversion (to generate an "image" from the detected signal)
6. A priori knowledge (to help the inversion or utilization)
7. "Image" utilization (generation of a useful output as an input for a decision making process)

In Table 1 these categories are further subdivided into descriptors that indicate important attributes or functions of the categories. These descriptors help guide our understanding of the extent of each category. (Notice that in Table I with respect to Figure 1 that the illumination has been incorporated into the scene as a descriptor and that a priori knowledge has been left out, but is intrinsic with many of the algorithms associated with inversion).

One way of utilizing Figure 1 and Table I is to track a particular system through the various categories and descriptors. For example let us consider the human visual system.

Illuminator:	Sun or other source of visible light
Scene:	Reflectivity and movement
Channel:	Atmospheric
Measurement System:	Collector; imaging lens (two) Detector; photoreceptive array (two) Platform; eyeball + head + body movement
Inversion:	Direct + binocular effects
A priori knowledge:	Relative scale of objects for depth cue
Utilization:	Mensuration, change (motion) detection, etc.

We certainly have not considered all the possibilities in the above example, but it does start us thinking in a systematic way about the system.

Table 1

**Discrimination/
Interpretation
Display**

Let us consider another example, namely, Aperture Synthetic Radio Astronomy.

Illumination:	None
Scene:	Self emissive, spatial incoherence
Channel:	Free space + atmosphere
Measurement System:	Collector; antenna array Detector; microwave sensor Platform; earth (rotation essential)
Inversion:	Fourier transform of correlation between sensor outputs to produce a sky brightness map (image)
A priori knowledge:	Non-negative sky brightness
Utilization:	Source distribution, mensuration
Reprocessing:	Strong source removal ("clean" algorithm)

In many respects this system is very different than the human visual system yet produces an "image." It would be informative to track through these categories and descriptors for other creature imaging systems, but I will leave the tracking up to those who are experts in such systems.

As indicated at the start, this paper was intended to stimulate thought about imaging and not necessarily present answers. However, some observations will be made here. It is clear that a priori information plays a key role in extending the capabilities of many systems that gather incomplete data sets. Modern computational capabilities often allow this a priori data to be used where it was impractical before. An example of this is iterative processing which constructs an image from only Fourier modulus data and a non-negativity constraint. Modern computational capabilities are often essential, as in the case of the Aperture Synthesis Radio Astronomy imaging example

given above. Typically, in this case an image is formed only after intensive data processing (inversion).

Are there other key elements?

APPENDIX C

LASER HETERODYNE RANGING USING A MODE-LOCKED LOCAL-OSCILLATOR FOR BANDWIDTH COMPRESSION*

Carl C. Aleksoff and L. M. Peterson

Abstract

It is shown that a mode-locked laser can be used as a local oscillator (LO) in heterodyne ranging to bandwidth compress the received signal. The amount of bandwidth compression depends on the difference in the intermode frequencies between the LO laser and the transmitter laser, which can also be a mode-locked laser. Since the heterodyning occurs on the detector, it is only necessary to use a narrow bandpass receiver that passes the compressed bandwidth to obtain ranging equivalent to that obtained by a wide bandwidth receiver that passes the full transmitter bandwidth. Bandwidth compression of over 500 times and one foot range resolution was experimentally demonstrated with a 1.5 GHz He-Ne laser mode-locked transmitter signal was reduced to less than 3 MHz at detection.

*Submitted to Optical Engineering for publication. Parts of this paper were also presented at the Los Alamos Conference on Optics '83 and published as "Bandwidth Compression Using a Mode-Locked Local Oscillator Laser" in the Proc. SPIE, Vol. 380, 1983, pp. 239-247.

Bandwidth Compression Using a Mode-Locked Local-Oscillator Laser

G.C. Aleksoff and L.M. Peterson

Environmental Research Institute of Michigan
Infrared and Optics Division
P.O. Box 8618, Ann Arbor, MI 48107

Abstract

It has been demonstrated in a laboratory experiment that a mode-locked laser can be used as a local oscillator (LO) in a heterodyne ranging system to sample or bandwidth compress the received signal. The bandwidth compression depends on the difference in the intermode frequency between the LO laser and the transmitter laser. Bandwidth compression of over 500 times was demonstrated, i.e., a 1.5 GHz He-Ne laser transmitter signal was reduced to 3 MHz upon detection. Since the mixing occurs on the surface of the detector only a narrow bandpass receiver that passes the compressed bandwidth is necessary to obtain ranging equivalent to that obtained by a wide bandwidth receiver that passes the full transmitter bandwidth.

Introduction

In laser ranging systems and in laser radar (LADAR) the resolution of the system improves as the bandwidth of the transmitted/received signal increases. Basically the best range resolution ΔR for a monostatic LADAR system is given by

$$\Delta R = \frac{c}{2B} \quad (1)$$

where c is the speed of light and B is the bandwidth of the transmitted/received signal. For a system that transmits pulses of width T , for example, using mode-locked lasers, then $B = T^{-1}$ can be substituted into Eq. (1). However, in general, pulses are not required and other waveforms such as linear chirp signals can be used to minimize peak power levels.

Typically, the larger the transmitted bandwidth the larger the detector and receiver bandwidths must be to utilize the signal and obtain the best resolution. However, the technique described in this paper alleviates the detector and receiver bandwidth requirement by taking advantage of the low bandwidth occupancy of mode-locked lasers. That is, lasers often emit only in discrete longitudinal modes with no emission between the modes. For a mode-locked laser the modes are phase locked together to form the pulses characterizing such lasers. Further, since the information (modulation) rate of return from a target is often low then this information can be redistributed to lie between the modes in such a way as to reduce the overall bandwidth requirements on the detector and receiver.

Basics

The technique, which we denote as differential mode-locked laser (DMLL) ranging, uses two separate mode-locked lasers. One mode-locked laser is the source of the transmitted energy and the other is used as the local oscillator (LO) in a heterodyne type of setup. Let $s_1(t)$ be the transmitted signal and $s_0(t)$ be the LO signal, and $S_1(f)$ and $S_0(f)$ their spectra (Fourier transforms), respectively. The signals are related by the Fourier transform relationship

$$S(f) = \int s(t) e^{-2\pi i f t} dt \quad (2)$$

The mode-locked spectral signals can be written as

$$S_0(f) = \sum_n a_n \delta(f - n f_0 - f_0 - \Delta f), \quad (3)$$

$$S_1(f) = \sum_n b_n \delta(f - n f_1 - f_0), \quad (4)$$

which has the time signal description

$$s_1(t) = \sum_n b_n \exp i 2\pi (n f_1 + f_0) t \quad (5)$$

where f_0 is an arbitrary center optical frequency, F_0 and F_1 are the intermode frequency differences for the LO and transmitter signals, respectively, a_n and b_n are the (complex) mode amplitudes of the LO and transmitter signals, respectively, and Δf is the LO offset frequency.

If $s_1(t)$ is transmitted and scattered off some target then the received signal $s_2(t)$ can be written as

$$s_2(t) = \sum_q c_q s_1(t - \tau_q) \quad (6)$$

where τ_q is the round trip delay time and c_q is the effective amplitude scattering coefficient associated with the q th scatterer of the target. In general, τ_q is a function of time if the target is moving. Substitution of Eq. (5) into Eq. (6) gives

$$s_2(t) = \sum_n h_n(t) b_n \exp[-2\pi i(f_0 + nF_1 + d)t] \quad (7)$$

where

$$h_n(t) = \sum_q c_q \exp[2\pi i(f_0 + nF_1)\tau_q + td] \quad (8)$$

In the above expressions, d is a frequency shift that accounts for the nominal Doppler shift of the target. The received complex spectrum is obtained by taking the Fourier transform (FT) of Eq. (7), which gives

$$S_2(f) = \sum_n b_n H_n(f - f_0 - nF_1 - d) \quad (9)$$

where $H_n(f)$ is the FT of $h_n(t)$. The quantity $H_n(f)$ describes the spectral spread of the n th mode due to the target. Typically, the spread is limited, and we assume that it is limited to a bandwidth W , i.e.,

$$H_n(f) = 0 \text{ for } |f| > \frac{W}{2} \quad (10)$$

The detected signal for sufficiently fast detector and receiver electronics is given by

$$\begin{aligned} i(t) &= |s_0(t) + s_2(t)|^2 \\ &= s_0^* s_0 + s_2^* s_2 + s_0^* s_2 + s_2^* s_0 \end{aligned} \quad (11)$$

where $*$ represents complex conjugation. The detected spectrum is then the FT of Eq. (11), which is

$$I(f) = X_{00} + X_{22} + X_{02} + X_{20} \quad (12)$$

where the correlation spectra are defined via

$$\begin{aligned} X_{mn} &= X_{mn}(f) = S_m^*(f) * S_n(f) \\ &\triangleq \int S_m^*(f') S_n(f' + f) df' \end{aligned} \quad (13)$$

After substitution of Eq. (3) and Eq. (9) the various correlation spectra are

$$X_{00} = \sum_n \sum_k a_n^* a_k S(kF_0 - nF_0 - f) \quad (14)$$

$$X_{22} = \sum_n \sum_k b_n^* b_k H_n^*(f - nF_1) * H_k(f - kF_1) \quad (15)$$

$$X_{20} = \sum_n \sum_k b_n^* a_k H_n^*(f - d + kF_0 - nF_1 - f) \quad (16)$$

$$X_{02}(f) = X_{20}^*(-f) \quad (17)$$

These correlation spectra are shown in Figure 1 for a simple illustrative case of two mode-locked lasers with just three equal amplitude modes, i.e.,

$$S_0(f) = \sum_{n=-1}^{+1} \delta(f - f_0 - nF_0 - \Delta f) \quad (18)$$

$$S_1(f) = \sum_{n=-1}^{+1} \delta(f - f_0 - nF_1) \quad (19)$$

and a return given by

$$S_2(f) = \sum_{n=-1}^{+1} \text{rect}[(f - f_0 - d - nF_1)/W] \quad (20)$$

The point to note is that under certain conditions the received spectra is available as a band compressed spectra within the detected spectra in the region $W/2 < f < F_1/2$, i.e., as illustrated in Figure 1(g) within the region labeled "bandpass" (compare with Figure 1(a)). To quantify this observation let

$$F_1 < F_0$$

$$H_n(f) = 0 \text{ for } |f| > W/2 \quad (21)$$

$$\Delta F = F_0 - F_1$$

$$f = F_1/4$$

The bandpass region f_{bp} then ranges from $W/2$ to $F_1/2$. We can get

$$N = \frac{F_1 - W}{2\Delta F} \quad (22)$$

modes into the passband without overlap. The limit is when we let $\Delta F = W$ then

$$N = \frac{F_1 - W}{2W} \quad (23)$$

If the above conditions are satisfied then we can bandpass the terms in Eq. (16) for which $n = k$ to obtain the real part of

$$S_1'(f) = \sum_n b_n^* a_n H_n(f_0' + n\Delta F - f) \quad (24)$$

where $\Delta F = F_0 - F_1$ and $f_0' = \Delta f - d$. Comparison of this Equation with Eq. (9) shows that all the desired terms are present, however there is a difference in that a weighting a_n exists and the frequency direction is reversed. The conjugation is not significant since the terms are separated and only the real part is used. The new carrier frequency f_0 and the new intermode spacing ΔF are controllable via Δf and F_0 . If the LO laser has uniform amplitude modes, i.e., $a_n = 1$, then the filtered output is exactly of the same form as $s_1(t)$ except time is reversed, which is not significant. What is important is that the signal mode spacing has been compressed by the ratio

$$C = \frac{F_1}{F_0 - F_1} \quad (25)$$

which is the desired result.

Experimental Results

The experimental setup is shown in Figure 2. Two He-Ne lasers were mode-locked to the frequencies F_0 and F_1 , which for the results presented were about 73.94 MHz and 73.80 MHz, respectively. The mode locking was accomplished via intracavity acoustic cells driven at half the mode lock frequency². The mode-lock difference frequency was $\Delta F = F_0 - F_1 = 140$ kHz. The signal derived from the mode lock RF oscillators via a mixer is half this

frequency and is used to synchronize the oscilloscope connected to the output detector. The laser operating at frequency F_1 was used as the transmitter source (its light illuminated the target), and the laser operating at frequency F_0 was used as the LO laser source. The LO laser had one of its cavity mirrors mounted on a piezoelectric translator in order to control the laser cavity length which determines the LO offset frequency Δf . A half wavelength change in cavity length allows a full 74 MHz of change in Δf . Both lasers were monitored by a high speed detector connected to sampling oscilloscopes and were also monitored via an optical spectrum analyzer.

Light scattered from the target was combined with the LO light by a beamsplitter and the two resulting combinations were detected with two detectors. One detector, a fast >2 GHz cutoff frequency detector, was connected to an electrical spectrum analyzer to observe the entire electrical spectrum, while the other detector, a slow <70 MHz cutoff frequency detector was fed to an oscilloscope via a filter to observe the desired filtered time signal. It is noted that this is a heterodyne technique and hence, that the wavefronts of the two light fields have to be aligned accurately.

Figures 3 and 4 show some of the results. Figure 3 presents the results for a target composed of a single point scatterer, and Figure 4 for two point scatterers separated by about 14 inches. Figures 3(a) and 4(a) show the time outputs of the two lasers. The pulse width of the mode-locked output was about 1 nsec. Figures 3(c) and 4(e) show the optical spectra of both lasers simultaneously. The resolution of the optical spectrum analyzer (~ 20 MHz) was not sufficient to separate out the two spectra for typical operation where the offset between the two spectra was about 10 MHz, such as for Figure 3(c). However, in Figure 4(e) the LO offset, Δf , was set (for observational purposes only) at about 37 MHz so that both sets of modes are distinguishable, i.e., each alternative peak corresponds to a mode of the same laser. Each laser oscillates in about 20 longitudinal modes spread over about 1.5 GHz. Thus, for direct observation of the laser signals and for ranging, the detector and receiver electronics need about 1.5 GHz of bandwidth. Indeed, the lower curve in Figure 4(f) shows direct ranging results using fast detectors and electronics for the two point scatterer case.

The lower trace in both Figure 3(b) and Figure 4(b) show the desired filtered time signal from the target after heterodyning with the LO light. Figure 4(c) shows the output after a rectification stage (compare with Figure 4(f)). Notice that the time scale is 2 $\mu\text{sec}/\text{div}$ in Figure 4(c) and 5 nsec/div in Figure 4(f). The comparison shows that the bandwidth compression (or time slowdown) is consistent with the expected ratio of $F_1/\Delta f = 500$. Notice the time reversal phenomenon in Figure 4(c). Although a GHz response detector is required to range resolve the two targets in Figure 4(f), only a MHz response detector is required in Figure 4(c).

Figure 5(a) shows part of the detected electrical spectrum for a single point target, similar to that shown in Figure 3(d) but on an expanded scale. Also, the mode-locked difference frequency Δf was increased to 538 kHz, which makes the individual modes more evident. Figure 5(b) shows the same spectrum but displayed using an acoustooptic (AO) spectrum analyzer setup composed of a 1 mW He-Ne laser beam illuminating a Bragg AO cell (~ 20 MHz bandwidth centered at 40 MHz), a lens to produce the FT, and a 1024 element linear detector array at the FT plane. The detected signal from the DMML setup was directly fed into the AO cell. The AO generated spectrum for the two point target case ($\sim 16''$ separation) is shown in Figure 5(c). The expected (~ 1 cycle) sinusoidal envelope on the individual cross-correlation spectra is clearly evident. Again a GHz bandpass phenomenon is displayed using a MHz bandpass device.

Conclusions

The concept of reducing the bandwidth requirements on the detector and receiver electronics for laser ranging applications has been demonstrated to be feasible by using a mode-locked transmitter laser and a mode-locked local oscillator laser.

This work was supported by the U.S. Army Research Office.

References

1. Cook, C.E. and M. Bernfeld, Radar Signals, Academic Press, N.Y., 1967.
2. Harerove, E. R.C. Ford, and M.A. Pollack, "Locking of HeNe Laser Modes Induced by Synchronous Intracavity Modulation," Appl. Phys. Lett. 5 (1964) pp. 4-5; A. Yariv, Quantum Electronics, Second Edition, 1975, John Wiley, New York.
3. Bachman, C.G., Laser Radar Systems and Techniques, Artech House, Dedham, MA., 1979

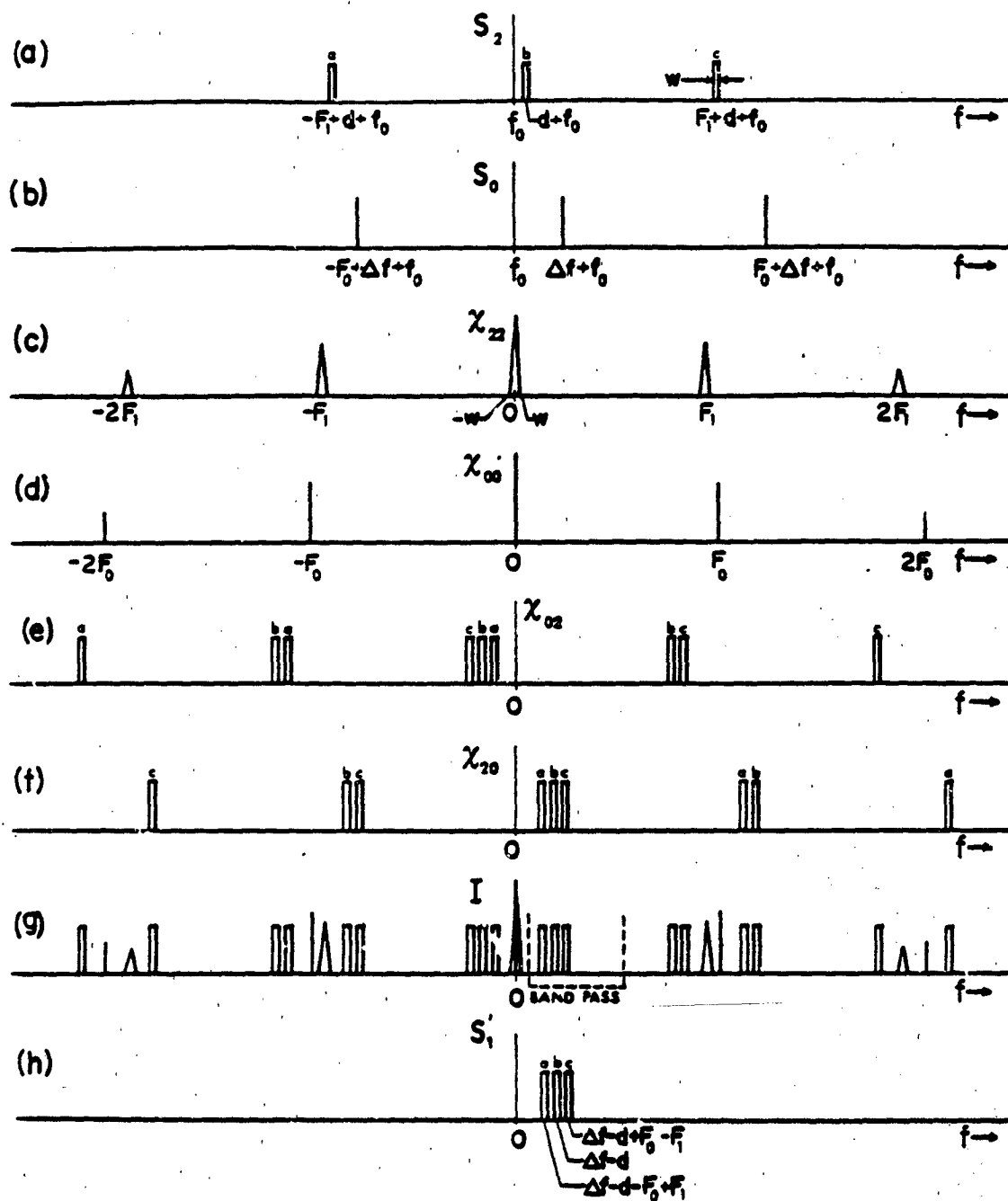


Figure 1. An example set of spectra for a 3-mode laser. (a) The target signal spectrum. (b) The local oscillator spectrum. (c) Target signal autocorrelation spectrum. (d) Local oscillator autocorrelation spectrum. (e) The χ_{02} cross-correlation spectrum. (f) The χ_{20} cross-correlation spectrum. (g) The total detection spectrum. (h) The output filtered spectrum.

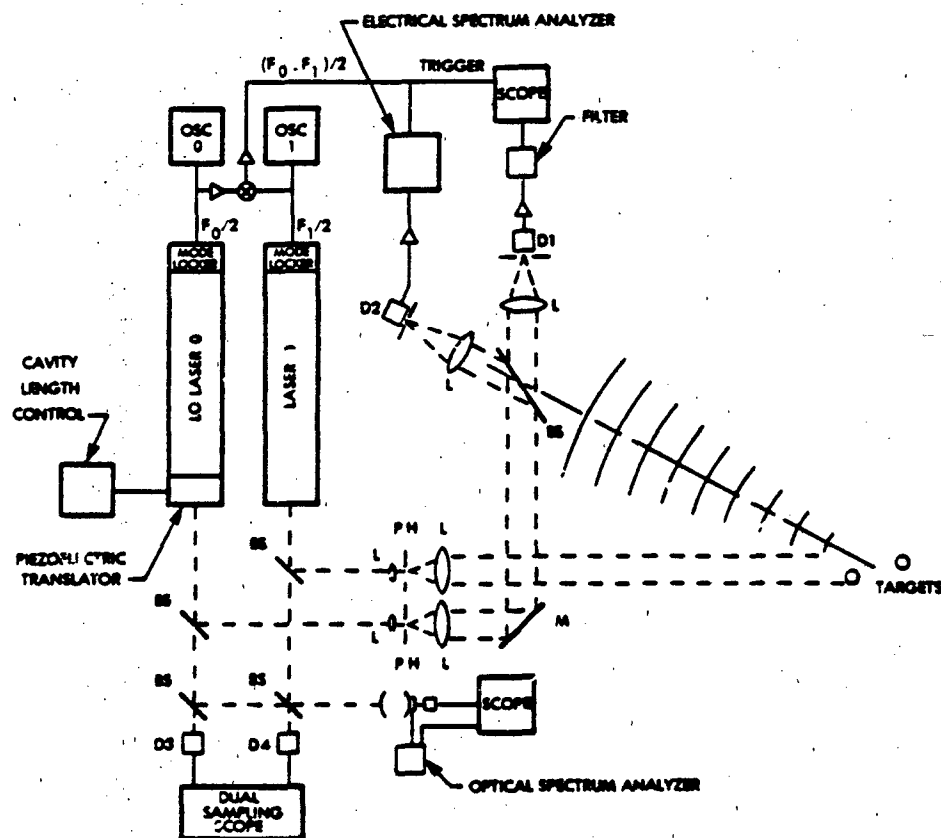


Figure 2. The experimental setup. OSC-oscillator, D-detector, BS-beamsplitter, L-lens, M-mirror, and PH-pinhole.

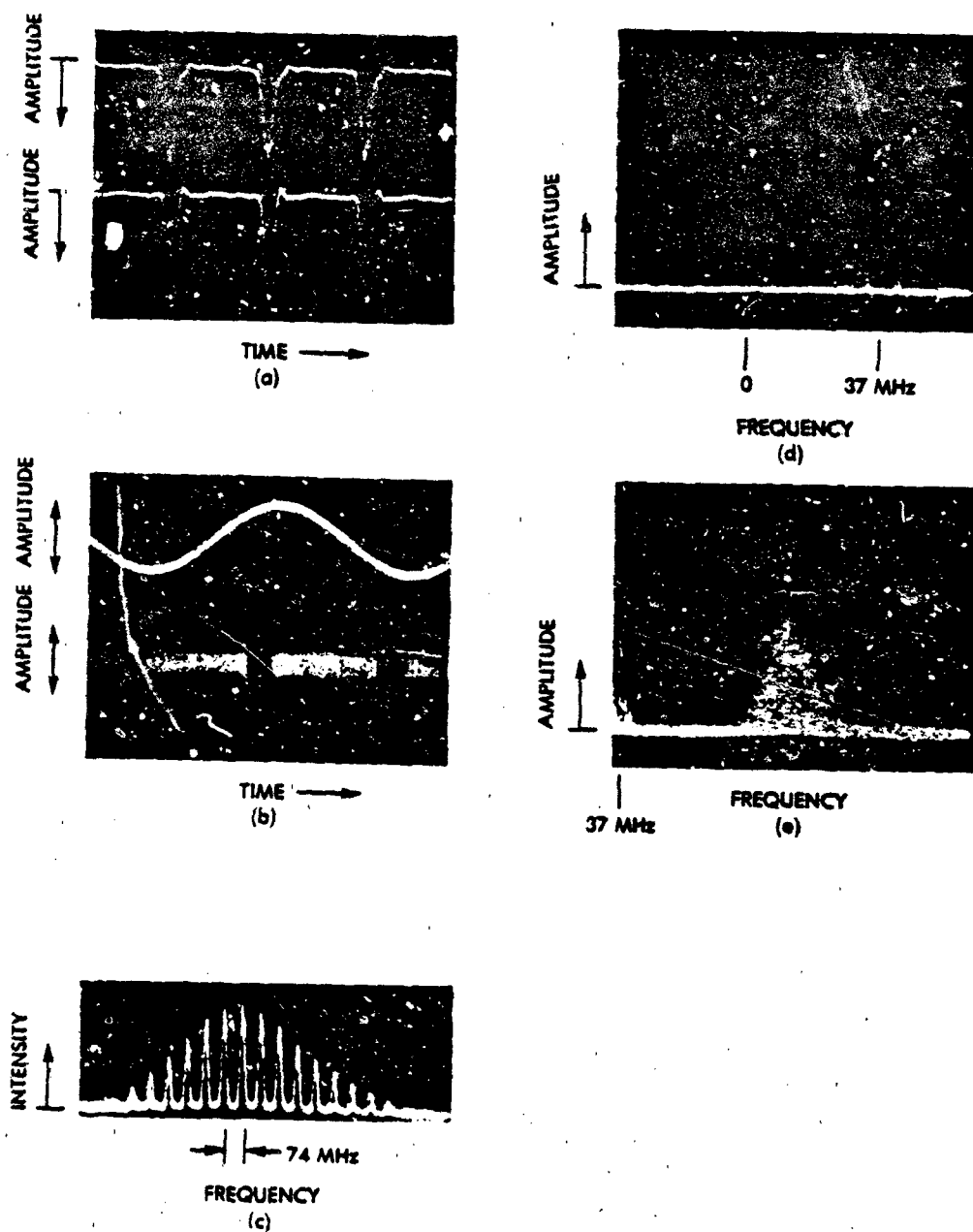


Figure 3. Experimental results for one point target. (a) The two He-Ne mode-locked laser outputs (fast detectors and sampling scope acquisition). (b) Top trace: the difference signal between the drive signals for the mode-locks. Lower trace: the received signal after heterodyning with the LO mode-locked laser light and bandpass filtering. (c) The optical spectrum of both lasers. (d) Part of the electrical spectrum of the detected signal. The spectrum to be filtered is centered at about 32 MHz or 42 MHz. (e) An expanded version of the electrical spectrum showing the part of the spectrum that can be bandpassed to obtain the desired output.

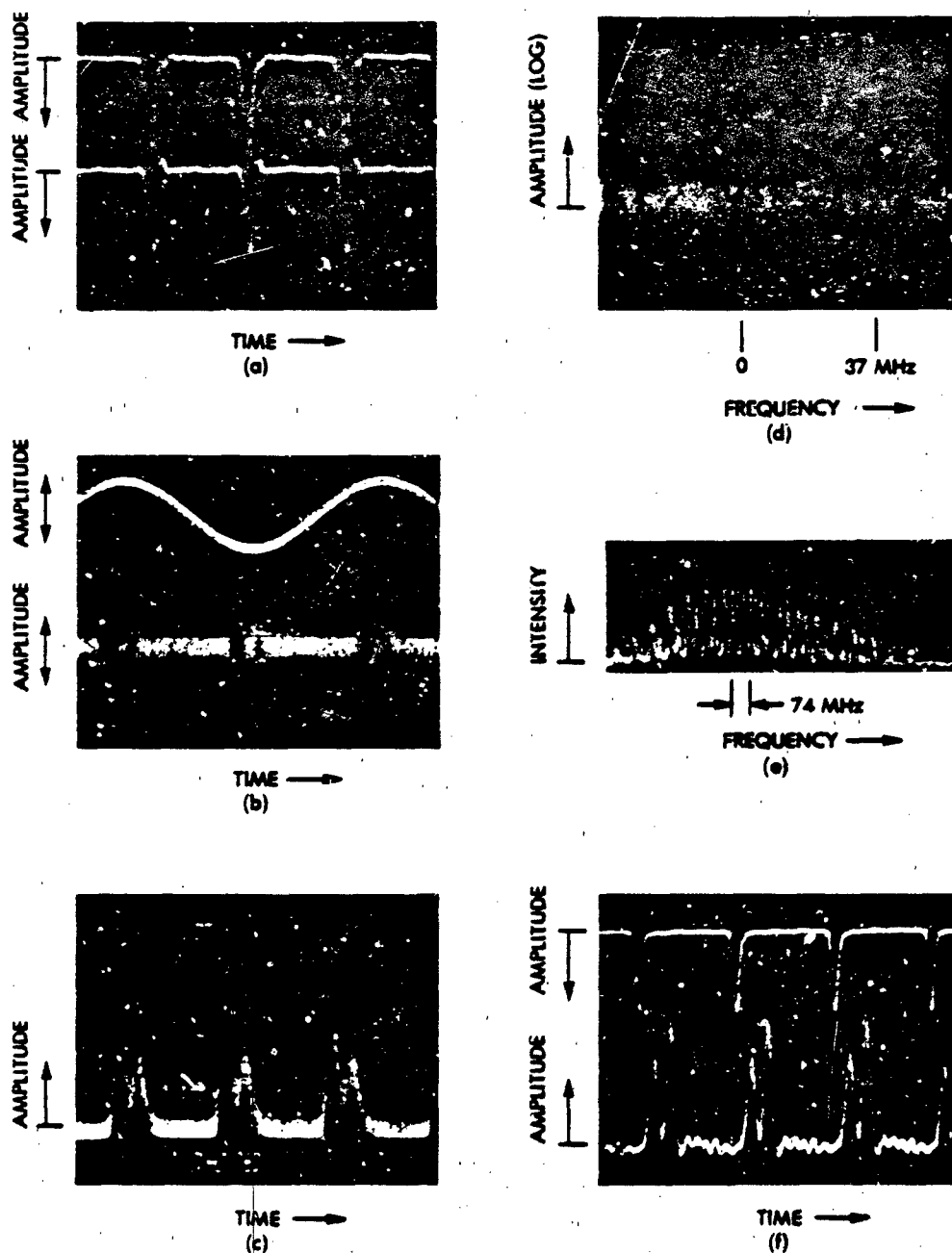


Figure 4. Experimental results for two point targets separated by 14 inches. (a) The two He-Ne mode-locked laser outputs acquired via fast detectors and a sampling oscilloscope. (b) Top trace: the difference signal between the drive signals for the mode lockers. Lower trace: the received signal after heterodyning with the local oscillator light and bandpass filtering. (c) The filtered signal after rectification. (d) Part of the electrical spectrum of the detected signal. The desired spectrum to be filtered is centered at about 27 MHz. (e) The optical spectrum of both lasers when the LO offset frequency is about 37 MHz. (f) Upper trace: the transmitted pulses. Lower trace: the received signal for direct detection with fast detectors and sampling scope acquisition for the case of two point targets.

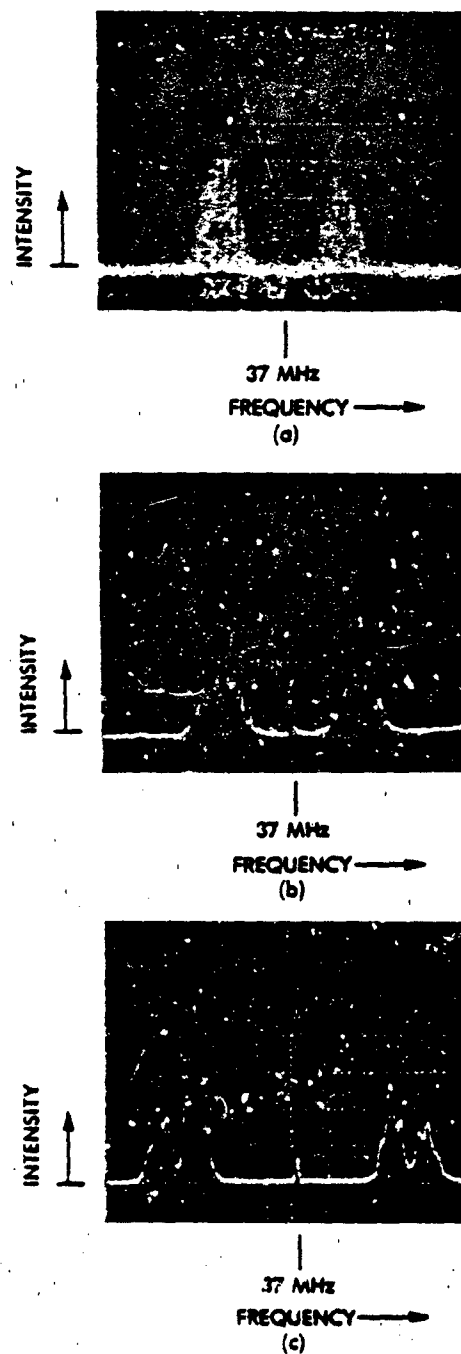


Figure 5. Electrical spectra of the detected signal. Horizontal scales for all the figures is 2.5 MHz/div and the mode-lock difference frequency is 538 kHz. (a) and (b) show a one point target response and (c) shows the response for two point targets with a 15 inch separation. (a) shows the response with a Tektronix 7L12 electronic spectrum analyzer. (b) and (c) are AO cell generated spectra. Measured resolution of the AO spectrum analyzer was 230 kHz.

APPENDIX D

TAPPED-FIBER SPECTRUM ANALYZER*

C. C. Aleksoff and T. M. Stachelek

Abstract

An optical spectrum analyzer was experimentally demonstrated that consisted of three main parts: (1) a periodically tapped optical fiber to produce a sampled one-dimensional spatial signal, (2) appropriate optics to produce a spatial Fourier transform, and (3) a holographic matched filter to (in effect) phase correct all the optical taps. Alternative potential configurations and signal processing operations are also presented.

*To be submitted to Optics Communications for publication.

APPENDIX E

OPTICAL-HYBRID BACKPROJECTION PROCESSING*

C. C. Aleksoff, I. J. LaHale and A. M. Tai

Abstract

In some synthetic aperture systems, the data gathered from a single transmitted pulse samples the 3-D frequency space of the object. A 3-D image can be formed by taking a 3-D FT on this data. However, the data are often in a form that allows backprojection techniques to be efficiently used to generate the image. We describe an optical hybrid coherent backprojection processing technique that uses a 1-D spatial light modulator, a coherent optical processor, a 2-D detector array, and some simple computer post-processing to produce the image.

*This paper was presented at the 10th International Computing Conference, "Unconventional Imaging and Unconventional Transformations" April 1983. Published in the Proc. SPIE, Vol 422, 1983, pp. 89-95

OPTICAL-HYBRID BACKPROJECTION PROCESSING

C. C. Aleksoff, I.J. LaHaie, and A.M. Tai

Environmental Research Institute of Michigan
Infrared and Optics Division
P.O. Box 8618
Ann Arbor, Michigan 48107

Abstract

In some synthetic aperture systems the data gathered from a single transmitted pulse samples the 3-D frequency space of the object. A 3-D image can be formed by taking a 3-D FT of this data. However, the data are often in a form that allows backprojection techniques to be efficiently used to generate the image. We describe an optical hybrid coherent backprojection processing technique that uses a 1-D spatial light modulator, a coherent optical processor, a 2-D detector array, and some simple computer post-processing to produce the image.

Introduction - Backprojection

In such radar and laser radar systems as spotlight synthetic aperture radar (SSAR) and those that image rotating objects, the construction of the 3-D image $U(\vec{x})$ can often be described, as will be shown later, by the 3-D FT (Fourier transform) [1-5]

$$U(\vec{x}) = \mathcal{F}_3\{u(\vec{f})\} \quad (1)$$

$$A \int u(\vec{f}) e^{-2\pi i \vec{f} \cdot \vec{x}} d\vec{f}$$

where $U(\vec{x})$ describes the (complex) image amplitude in coordinates $\vec{x} = (x, y, z)$ of the image and $u(\vec{f})$ describes the available (complex) data in coordinates $\vec{f} = (f_x, f_y, f_z)$ of spatial frequency space. We can write

$$u(\vec{f}) = a(\vec{f}) u_0(\vec{f}) \quad (2)$$

and

$$u_0(\vec{x}) = \mathcal{F}_3\{u_0(\vec{f})\} \quad (3)$$

where $u_0(\vec{f})$ represents the spatial frequency description of the ideal image $U_0(\vec{x})$ over all of space and $a(\vec{x})$ represents the 3-D aperture over which the data was gathered. Often the data only lies on some 3-D surface, as will be shown later for some specific examples. In any case, the actual reconstructed image can be described as the 3-D convolution of the spread function with the ideal function as given by

$$U(\vec{x}) = U_0(\vec{x}) *** A(\vec{x}) \quad (4)$$

where

$$A(\vec{x}) = \mathcal{F}_3\{a(\vec{f})\} \quad (5)$$

is the 3-D spread function and $***$ represents a 3-D convolution. We note that an active area of research is the extending of the aperture by filling in the frequency data, e.g., interpolation and/or extrapolation, but our only consideration in this paper is to use the data directly [6].

Often the data can be described as being gathered along straight lines that go through the origin, which we will call polar lines. Let $L(\vec{f}, \hat{b})$ define a polar line (of delta width) in the direction of the unit vector \hat{b} . Now we note that the 3-D FT of a polar line is a plane through the origin, which we will call a polar plane [7,8]. Namely, we have

$$P(\vec{x}, \hat{b}) = \mathcal{F}_3\{L(\vec{f}, \hat{b})\} \quad (6)$$

where $P(\vec{x}, \hat{b})$ describes a polar plane with delta support in the direction of its normal \hat{b} .

Now we consider the case where the data in frequency space lies along polar lines as can be described by

$$u(\vec{f}) = \sum_n u'_0(\vec{f}) L(\vec{f}, \hat{f}_n) \quad (7)$$

where

$$u'_0(\vec{f}) = u_0(\vec{f}) a'(\vec{f}). \quad (8)$$

Here, $a'(\vec{f})$ is the part of the aperture function describing the support of the data along polar lines orientated in the direction, \hat{f}_n , i.e., the total aperture description is

$$a(\vec{f}) = a'(\vec{f}) L(\vec{f}, \hat{f}_n). \quad (9)$$

The image, i.e., the FT of $U(\vec{r})$ as given by Eq. (7), can be written as

$$U(\vec{r}) = \sum_n \tilde{U}_0'(\vec{r}_n) \quad (10)$$

where

$$\tilde{U}_0'(\vec{r}_n) = U_0'(\vec{r}) *** P(\vec{r}, \hat{x}_n) \quad (11)$$

$$= \int U_0'(\vec{q}) \delta(\vec{r} - \hat{x}_n \cdot \vec{q}) d\vec{q},$$

$$U_0'(\vec{r}) = U_0(\vec{r}) *** A'(\vec{r}) \quad (12)$$

and $\vec{r}_n = x\hat{x}_n, \vec{f}_n = f\hat{f}_n$ such that

$$\hat{x}_n \cdot \hat{f}_n = 1 \quad (13)$$

The quantity $\tilde{U}_0'(\cdot)$ described by Eq. (11) is known as the Radon Transform of $U_0'(\cdot)$, and is obviously just the integration of U_0' over planes, i.e., the convolution operation of U_0' with $P(\cdot)$. The values of U_0' for fixed \hat{x}_n is described as projections of $U_0'(\cdot)$ [7]. Thus, we see that the final image formed with this data can be considered as the sum of the Radon transforms of the ideal image convolved with the partial spread function $A'(\cdot)$.

Let us now go back to Eq. (7) and derive the operational FT form that we seek. Since $L(\cdot)$ is a line delta function we can write

$$u(\vec{r}) = \sum_n u_0(\vec{r}_n) a'(\vec{r}_n) L(\vec{r}, \hat{f}_n), \quad (14)$$

emphasizing the one dimensional nature of each line of data by using $\vec{f}_n = f\hat{f}_n$, where it is understood that \hat{f}_n is a fixed unit vector. Hence, the 3-D FT of $u(\vec{r})$ can then be written as

$$U(\vec{r}) = \sum_n W_n(x) L(\vec{r}, \hat{x}_n) * P(\vec{r}, \hat{x}_n) \quad (15)$$

where

$$W_n(x) = \mathcal{F}_1\{u_0(\vec{r}_n) a'(\vec{r}_n)\} \quad (16)$$

and

$$\hat{x}_n \cdot \hat{f}_n = 1$$

The quantity $W_n(\cdot)$ is the one dimensional FT along the n th polar line. The operation described by Eq. (15) is known as backprojection and has the simple geometrical understanding illustrated in Figure 1. Each 1-D FT is backprojected along a line normal to \hat{x}_n and intersecting the desired reconstruction point \vec{r} . Thus, we can write very simply that

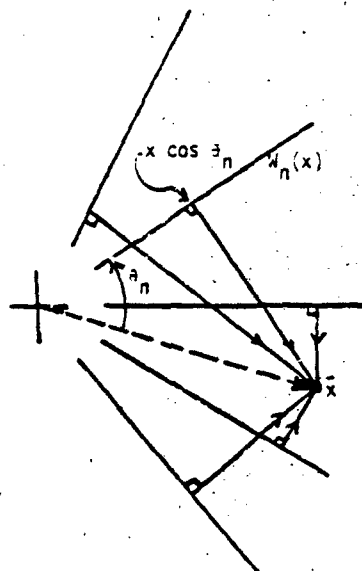


Figure 1. The Backprojection Technique

$$U(\vec{r}) = \sum_n W_n(x \cos \theta_n) \quad (17)$$

where θ_n is the angle between vector to the desired reconstruction point \vec{r} and the polar line direction \hat{x}_n . Thus, it is only necessary to sum backprojected scaled 1-D FTs. We will demonstrate this type of processing optically in a later section, although not for the 3-D case but rather for the 2-D polar distributed data. However, the concept is viable for the full 3-D case.

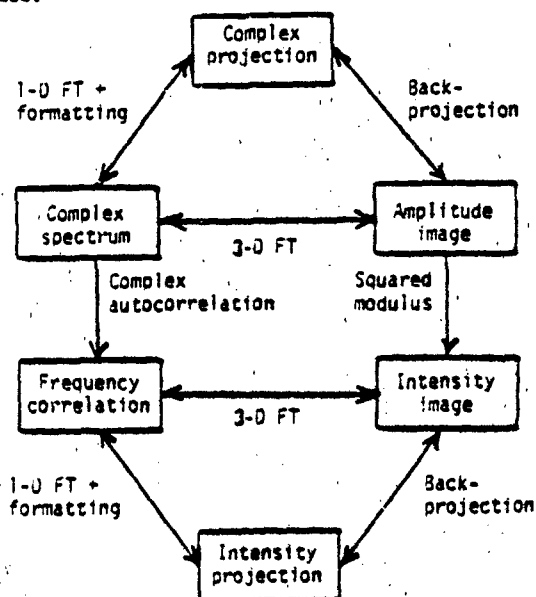


Figure 2. Image Transform Relationships

Figure 2 shows a block diagram of ways to reconstruct an image. In coherent systems the data and image can be complex whereas in interferometric or tomographic systems the image is nonnegative. The advantage of going along a backprojection path rather than a FT path is for computational saving. For example, the use of the FFT in digital processing requires the data to be on a parallelepiped grid, which implies that if the data not fall on the grid points that interpolation is necessary. The interpolation computational burden can often exceed the FFT computational requirements by many orders of magnitude and makes the FFT based technique unattractive.

There is also a difference as to where the data are gathered. In tomography the projections are the basic entity gathered whereas in synthetic aperture systems frequency space data are usually the basic entity gathered.

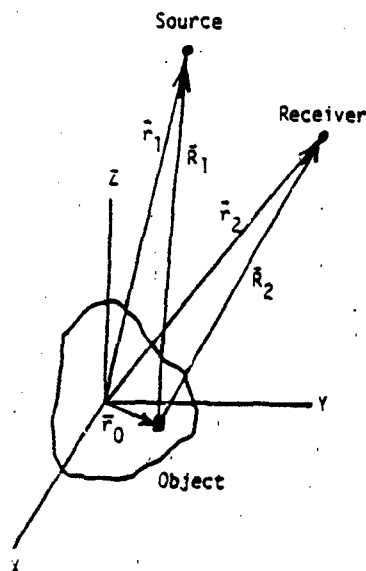


Figure 3. Bistatic Imaging System Geometry

Synthetic Aperture Basics

Consider a coherent bistatic synthetic aperture imaging system that illuminates an object or scene from position \vec{r}_1 and receives the return at position \vec{r}_2 . See Figure 3. The coordinate system is assumed fixed with respect to the object. For a monochromatic scalar E-field (analytic signal) description, the received signal from a differential element scatterer at \vec{r}_0 is given by (within a complex constant multiplier)

$$1S(\vec{r}_0) = -(\vec{r}_0)kR_1^{-1} \exp(ikR_1)kR_2^{-1} \exp(ikR_2)d\vec{r}_0 \quad (13)$$

where $\gamma(\vec{r}_0)$ is the scattering coefficient, k the wave number

$$k = \frac{2\pi}{\lambda} = \frac{2\pi\nu}{c}, \quad (19)$$

ν the temporal frequency and $R_i = |\vec{r}_i - \vec{r}_0|$. Integrating over the object (all the scatterers) gives

$$S = k^2 \int \frac{\gamma(\vec{r}_0) e^{ik(R_1+R_2)}}{R_1 R_2} d\vec{r}_0. \quad (20)$$

In the far field we can let

$$R_i = |\vec{r}_i - \vec{r}_0| = r_i - \vec{r}_0 \cdot \hat{r}_i \quad (21)$$

in the exponent and let $R_i = r_i$ in the denominator to get

$$S = \frac{k^2}{r_1 r_2} e^{ik(r_1+r_2)} \int \gamma(\vec{r}_0) e^{-2\pi i \vec{f}_0 \cdot \vec{r}_0} d\vec{r}_0 \quad (22)$$

and

$$\vec{f} = \frac{1}{\lambda} (\hat{r}_1 + \hat{r}_2) = \frac{\nu}{c} (\hat{r}_1 + \hat{r}_2) \quad (23)$$

Eq. (22) is a basic result which states that the received signal is proportional to the 3-D FT of the object scattering function when the spatial frequency is properly interpreted.

We would like to invert Eq. (22) to find γ from S . In the cases of our interest the inversion is helped by the fact the frequency ν is centered about some carrier frequency, and hence the effect of k^2 is reasonably constant enough to ignore. Furthermore, the rate of change of ν is small enough to allow the above first order (quasi-CW) analysis. Also, r_1 and r_2 do not typically vary enough to have to be taken into account other than in the exponent where the variation of $k(r_1 + r_2)$ is significant. In fact, to account for this factor the received signal is multiplied by a function proportional to $\exp[-ik(r_1 + r_2)]$ to remove its effect and truly establish what is known as a MCP (motion compensation point) in space fixed with respect to the object. The MCP corresponds to the coordinate center of our frequency space. Thus, with these modifications and understandings, we can say that the image (estimate of the scatterers) is given by

$$\gamma(\vec{r}_0) = \int S(\vec{f}) e^{2\pi i (\vec{f}_0 \cdot \vec{r}_0)} d\vec{f} \quad (24)$$

where the integral is evaluated over the support of the available data points in frequency space, i.e., over the 3-D synthetic aperture. Notice that the aperture is created by changes in the spatial frequency \vec{f} as determined by the parameters \vec{r}_1 , \vec{r}_2 , or ν .

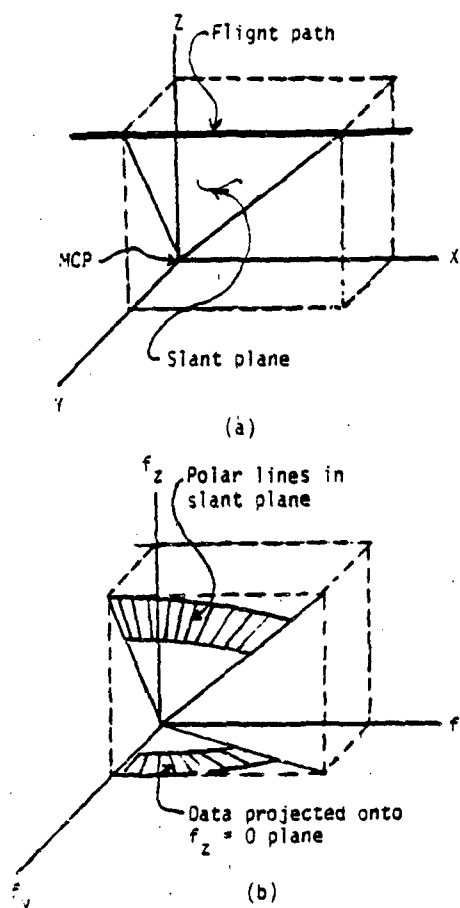


Figure 4. Spotlight Synthetic Aperture Radar. (a) Acquisition geometry. (b) Data distribution in frequency space.

Imaging System Examples

Consider a SSAR (Spotlight Synthetic Aperture Radar) where the aircraft carrying the radar flies along a straight path and keeps the radar pointed to the same area. The radar transmits FM linear chirp waveforms and also receives the returns. Thus, Eq. (24) holds and Eq. (23) becomes

$$\vec{r} = 2\vec{r}_0/c \quad (25)$$

where $r = r_1 = r_2$ for this case. If the radar frequency is chirped from ν_1 to ν_2 , then, as given by the above equation, the frequency vector direction is stationary but the vector magnitude varies from f_1 to f_2 , where $f_i = 2\vec{r}_0\nu_i/c$. Typically, the chirp pulses are short enough for \vec{r} not to change significantly due to the aircraft motion. Thus, we see that each chirp produces a section of a polar

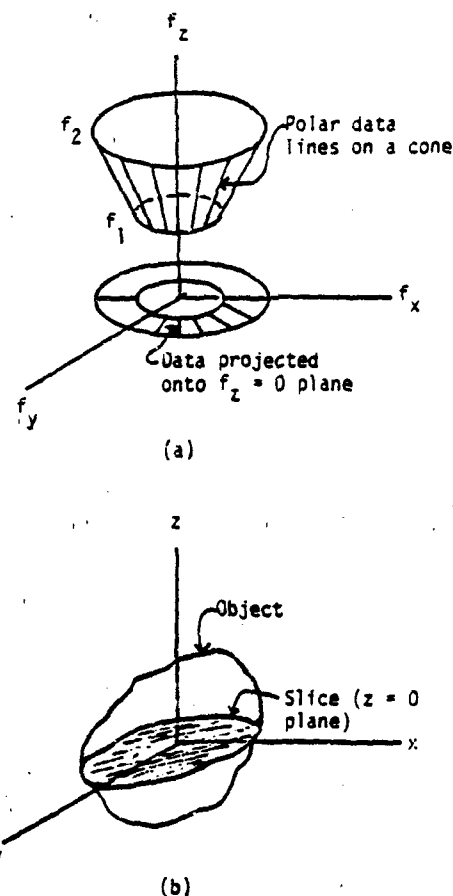


Figure 5. Imaging a Rotating Object. (a) Data distribution in frequency space and projection of the data onto the $f_z = 0$ plane. (b) Resulting image slice due to 2-D FT processing projected data of Fig. 5(a).

line of data in frequency space corresponding to the line of sight direction to the motion compensation point, as indicated in Figure 4. All the polar lines lie in a plane, called the slant plane, since the radar is traveling along a straight line. The general 3-D problem can be considered here to degenerate into a 2-D processing problem since all the data lies in a plane, i.e., the aperture is in the slant plane, and hence the spread function is infinitely long in the direction perpendicular to the slant plane. Thus, the image is at best a 2-D projection of the 3-D ideal image onto the slant plane. The required processing is simply a 2-D FT of the polar formatted data.

Let us consider the case of a fixed radar imaging a rotating object. Let the radar transmit FM linear chirps from frequency ν_1 to ν_2 . In our coordinate system fixed to the object the radar appears to move around the target in a circular path. Placing the motion compensation point on the object rotation axis produces polar

lines of data that lie on the surface of a cone as illustrated in Figure 5a. The finite chirp truncates the cone surface between radii of f_1 and f_2 , where $f_i = v_i(r_1 + r_2)/c$. The spread function for a truncated cone tends to look like a hollow cone. Typically, the 3-D frequency space data can be projected onto the $f_z = 0$ plane, producing a 2-D polar formatted signal which can be processed with a 2-D FT to obtain a slice ($z = 0$ plane) of the object. See Figures 5a and 5b. Scatterers that are not in the slice plane will produce rings instead of points, i.e., slices of the spread function [1].

Optical Backprojection Processing

In the previous section some examples were given as to how 2-D polar formatted input signals can be generated. Figure 6 shows the classical technique for optically processing such an input. The polar lines of data with a polar offset spatial frequency carrier are written onto a 2-D spatial modulator, e.g., density modulated photographic film. The signal is then coherently illuminated and the FT is taken optically to produce the usual conjugate images. One of the images is then detected for further analysis.

In its simplest terms this process can be described by writing the input as

$$v(\vec{r}) = B + 2 \sum_n |u_n(\vec{r})| \cos(2\pi\vec{r} \cdot \vec{h} + \phi_n) \quad (26)$$

where B is the bias, h the polar offset vector, and

$$u_n(\vec{r}) = |u_n(\vec{r})| \exp[i\phi_n(\vec{r})] \quad (27)$$

are just the individual terms of the summation given on the right hand side of Eq. (14). Notice in this section that the coordinates and vectors are all understood to be 2-D rather than 3-D as in the earlier sections. After the FT by the lens the processor output amplitude is given by

$$V(\vec{x}) = B\delta(\vec{x}) + \sum_n U_n(\vec{x} - \vec{h}) + U_n^*(\vec{x} + \vec{h}) \quad (28)$$

where $U_n(\cdot)$ is the FT of $u_n(\cdot)$ and $*$ represents conjugation. We can identify $U_n(\cdot)$ with the terms in the summations in Eq. (10) or Eq. (15). That is, $U_n(\cdot)$ simply represents the n th backprojection and such backprojections occur naturally in this system due to the input-formatting and the FT operation. The offset vector \vec{h} is picked to separate the two images away from the zero order. Detection of one of these images gives

$$I(\vec{x}) = \left| \sum_n U_n(\vec{x} - \vec{h}) \right|^2 \quad (29)$$

which is the desired result.

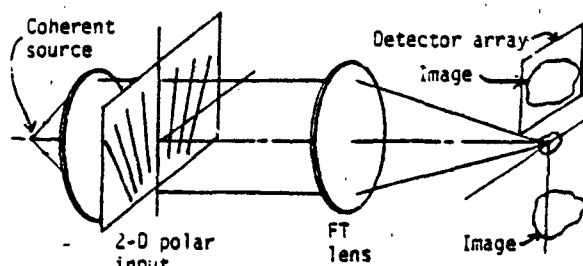


Figure 6. Classical Technique for Optically FT Processing Polar Formatted Data

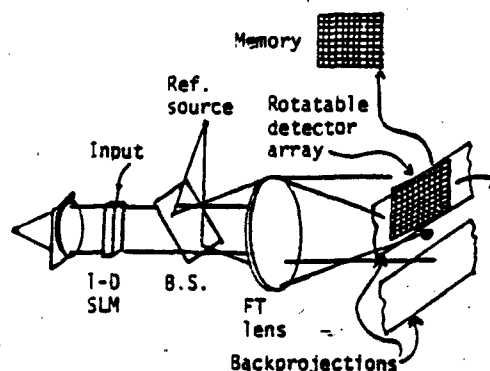


Figure 7. The Optical Backprojection Processor

In the above technique all the input data, lines are 2-D FTed simultaneously in parallel and coherently summed at the output to produce the image. An alternative technique, which we call the backprojection technique, is to 2-D FT each line sequentially (in real time) and then coherently sum them in a memory as is illustrated in Figure 7. The detector is rotated to the proper angle for each input line. The motivation for this alternative technique is to avoid 2-D spatial modulators, which are too limited in their capabilities for our use, and instead take advantage of the newly developing technology of spatial detector arrays and the mature technology of 1-D modulators, such as acousto-optic cells.

The backprojection technique can be described by letting the input be given by

$$v_n(\vec{r}) = B + C\delta(\vec{r}) e^{i\gamma} + 2 |u_n(\vec{r})| \cos(2\pi\vec{r} \cdot \vec{h} + \phi_n) \quad (30)$$

where $C\delta(\vec{r})e^{i\gamma}$ is the reference wave (a phase controllable point source at the origin of the input plane). The output of the processor (a 2-D FT) is given by

$$V_n(\vec{x}) = B\delta(\vec{x}) + C e^{i\gamma} + U_n(\vec{x} - \vec{h}) + U_n^*(\vec{x} + \vec{h}) \quad (31)$$

The detected signal, for one of the image terms plus the reference wave is

$$\begin{aligned} I_n(\bar{x}, \gamma) &= \left| C e^{i\gamma} + U_n(\bar{x} - \bar{h}) \right|^2 \\ &= C^2 + \left| U_n(\bar{x} - \bar{h}) \right|^2 \\ &\quad + C \left| U_n(\bar{x} - \bar{h}) \right| \cos(\gamma + \phi_n) \end{aligned} \quad (32)$$

Only the last term of this expression is desired. It can be isolated by using the reference wave phase. Note that

$$I_n(\bar{x}, 0) - I_n(\bar{x}, \pi) = 2C U_n(\bar{x} - \bar{h}) \cos \phi_n \quad (33)$$

$$I_n(\bar{x}, \frac{\pi}{2}) - I_n(\bar{x}, -\frac{\pi}{2}) = 2C U_n(\bar{x} - \bar{h}) \sin \phi_n$$

Thus, we can obtain the quadrature components (I and Q) by shifting the reference wave by $\pi/2$ increments for each line input and then subtracting the correct components. The subtraction is done digitally and the results are stored in a digital memory. The detector (or input) is rotated to the next position and the procedure is repeated. The running sums of the I and Q components are kept and the image at any time can be calculated as the sum of the squares of I and Q to give

$$I(\bar{x}) = 4C^2 \sum_n \left| U_n(\bar{x} - \bar{h}) \right|^2 \quad (34)$$

which is the desired result. See Eq. (29).

Experimental Setup

The actual experimental implementation differed from the conceptual description given above and tended to be set up as shown in Figure 8. The experiment was performed in non-real time, and for convenience, the 1-D data lines were generated by imaging a narrow slit onto a 2-D photographic recording of the polar formatted spatial frequency data. The input data and image plane were held stationary relative to each other; the rotation of each polar slice was achieved instead by rotating the slit. The total processed aperture was determined by the number of slices coherently summed and the width of the slit, both of which were allowed to vary. The advantage of this setup was that by fully opening up the slit a classically processed coherent image could be generated and directly compared to the image processed from projections.

The image plane data was sampled using a CID array camera. The required subtractions for the in-phase and quadrature (I and Q) components were performed on a desk-top computer which received the digitized data from the CID array. The phase shifts were introduced into the reference wave by monitoring the fringes caused by the interference of the reference beam and the undiffracted (DC) portion of the object beam with a pair of detectors whose spacing matched that of

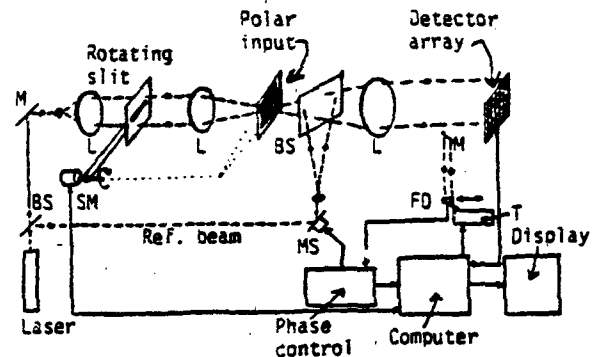


Figure 8. The Experimental Setup to Demonstrate Optical Backprojection Processing. Notation: L - lens, T - translator, SM - stepper motor, BS - beamsplitter, M - mirror, and FT - fringe detector. Solid lines are electrical, dashed are optical, and dotted are mechanical connectors.

the fringes. The detectors were operated in a difference mode, and their output used to drive a lock-in amplifier. The output of the lock-in amplifier was used to control a piezoelectric mirror in the reference beam path. In this manner, a feedback loop was created which served to "freeze" the fringe pattern onto the detector pair, i.e., to keep the relative phase between the object and reference waves steady. By moving the detector pair laterally across the fringe pattern, this "freezing" effect shifted the reference wave phase by a controllable amount. The same feedback loop also served to remove slowly-varying fluctuations in the relative phase of the two beams, which is also necessary for proper performance of the experiment.

The data acquisition and system control functions are performed electronically by both analog and digital equipment. The overall system is controlled by a Tektronix 4054 Graphics System Computer. Image data from a GE TN2500 camera in standard interlaced-field TV format is digitized by a CVI model 270 frame grabber, and these are supplied in digital form to the 4054 via a dedicated interface. The data is stored by the 4054 in an auxiliary memory capable of holding two full 16-bit grey level images ($2 \times 256^2 \times 16$).

The system reads four images into the graphics computer for each position of the aperture slit, with relative phases of 0° , 180° , 90° , -90° in the reference beam, and performs the necessary calculations to generate the I and Q images containing the desired information. The aperture is then rotated by a specified amount, and the procedure repeated. Running sums of the I and Q images are kept in the memory.

The data collection (i.e., image formation processing) did not run in real time, requiring approximately 45 seconds per subaperture. An image generated from 64 projections therefore requires about 45 minutes of run time.

A Basic Result

A basic result is presented in this section for a single point target, which serves to represent the "impulse response" of the backprojection processing algorithm.

Figures 9a-9c show experimental results for the reconstruction of the point target. In all cases, the length of the slit in the radial (range) direction is 18 mm. Figure 9a is a perspective plot of the impulse response of the slit, which in this case has a width of 0.2 mm. This can be viewed as a single backprojection. Figure 9b shows a plot of the image obtained by backprojection processing of 64 subapertures. The "compression" relative to Figure 9a is quite obvious. The effective total aperture is 18 x 12.8 mm. Figure 9c is a plot of the point target image produced using a real aperture of the same dimensions.

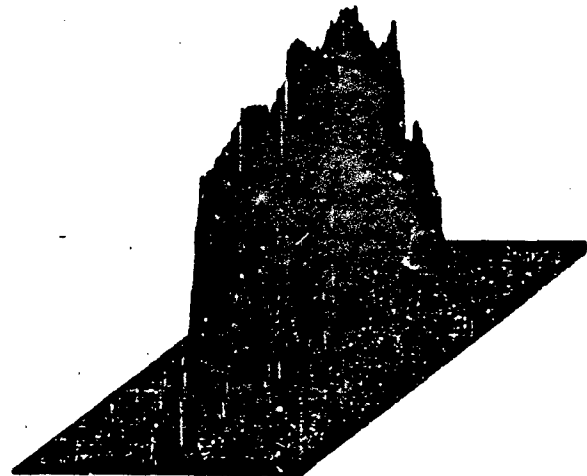
Conclusions

It was shown that backprojection processing can be a viable processing technique for cases where the Fourier frequency space of an object is sampled along polar lines. Imaging radar examples were presented that were characterized by data along polar lines. The concept of an optical-hybrid backprojection processor was successfully demonstrated experimentally. The potential for using a 1-D spatial light modulator as part of a real time system makes the technique very attractive.

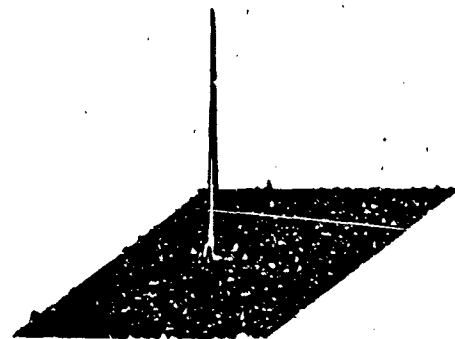
This work was supported in part by the U.S. Army Research Office.

References

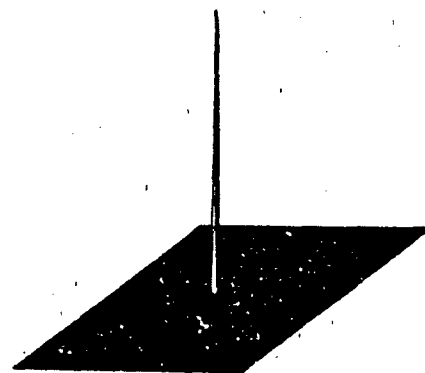
1. J.L. Walker, "Range Doppler Imaging of Rotating Objects," IEEE Trans. AES, Vol. 16, 23, Jan. 1980.
2. W.M. Brown, "Walker Model for Radar Sensing of Rigid Fields," IEEE Trans. AES, Vol. 16, 104, Jan. 1980.
3. C.C. Aleksoff, "Interferometric Two-Dimensional Imaging of Rotating Objects," Optic Letters, Vol. 1, 54, August 1977.
4. C.C. Chen and H.C. Andrews, "Target-Motion-Induced Radar Imaging," IEEE Trans. AES, Vol. 16, 2, Jan. 1980.
5. J.C. Kirk, "Motion Compensation for Synthetic Aperture Radar," IEEE Trans. AES, Vol. 11, May 1975.
6. J.R. Fienup, "Reconstruction and Synthesis Applications of an Iterative Algorithm," in Transformations in Optical Signal Processing, Ed. W.T. Rhodes, J.R. Fienup, and S.E.A. Saken, SPIE, 1983.
7. MY Chin, H.H. Barrett and R.G. Simpson, "Three-Dimensional Reconstructions from Planar Projections," JOSA, Vol. 75, July 1980.
8. R.M. Bracewell, The Fourier Transform and its Applications, McGraw-Hill, 1965.



(a)



(b)



(c)

Figure 9. Experimental Results for a Point Target. (a) Single backprojection. (b) Coherent summation of 64 backprojections. (c) Classical image with an aperture equivalent to Fig. 9(b). Horizontal scale for all figures is the same, but intensity (vertical scale) is arbitrary.

APPENDIX F

GRATING-BASED INTERFEROMETRIC PROCESSOR FOR REAL-TIME OPTICAL FOURIER TRANSFORMATION*

Anthony M. Tai and Carl C. Aleksoff

Abstract

A processing approach is introduced that is capable of performing 1-D real-time Fourier transformations on the intensity distribution of an incoherent optical input. The processing approach is based on grating interferometers, and the resulting processors are simple in structure and easily implemented. Possible processor configurations together with experimental results demonstrating the operations of the system are presented. Analyses are given comparing the grating interferometric processor to the Michelson stellar interferometer and the classical coherent optical processor.

*This paper was published in Applied Optics, Vol. 23, No. 14, 15 July 1984, pp. 2282-2291. This work was also supported by ARO Contract DAAG29-82-K-0173. Part of this work was also published in the Proc. SPIE, Vol. 422, pp. 99-104.

Grating-based interferometric processor for real-time optical Fourier transformation

Anthony M. Tai and Carl C. Aleksoff

A processing approach is introduced that is capable of performing 1-D real-time Fourier transformations on the intensity distribution of an incoherent optical input. The processing approach is based on grating interferometers, and the resulting processors are simple in structure and easily implemented. Possible processor configurations together with experimental results demonstrating the operation of the system are presented. Analyses are given comparing the grating interferometric processor to the Michelson stellar interferometer and the classical coherent optical processor.

I. Introduction

The Fourier transformation is a basic operation in many signal processing applications, and it has been implemented by various optical techniques. Coherent optical processors¹ can perform Fourier transformation in real time, but they have several familiar limitations. Most coherent optical processing schemes require the use of an incoherent-to-coherent converter which reduces the system speed, dynamic range, and linearity. An achromatic Fourier transform system^{2,3} can be utilized to relax the temporal coherence requirement and improve the system SNR by reducing coherence noise. The spatial coherence requirement, however, is unchanged, and an incoherent-to-incoherent converter is still needed.

One-dimensional processing using bulk acoustical modulators or SAW devices,^{4,5} on the other hand, are often too limited in their space-bandwidth product by physical constraints such as transducer frequency response, acoustical velocity, and acoustical attenuation. Moreover, processing with an acoustical modulator is limited to serial inputs. To be able to process parallel spatial inputs such as images, a spatial-to-temporal conversion is needed.

Incoherent optical processing techniques such as OTF synthesis^{6,7} permit the use of incoherent optical inputs, but their applications are limited to a rather

restrictive class of operation. For example, complex Fourier transformation has not been demonstrated. Cosinusoidal transformation was demonstrated by Mertz and Rogers⁸ using a shadow casting technique. Such a technique operates in the geometric optics regime, and the achievable space-bandwidth is consequently small. The optical vector-matrix multiplier^{9,10} can be configured to perform Fourier transformation; unlike other more conventional optical processors, the vector-matrix multiplier operates on discrete sampled signals. The difficulties in constructing and aligning a large 2-D mask and the limits on the densities of these masks restrict the space-bandwidth product that can be achieved in practice. The relative complexity of the system also diminished its attractiveness.

In this paper, we introduce an optical processor which belongs to a class of processor which we call interferometric processors. This processor operates on incoherent optical inputs, but its performance is closely related to coherent optical processing systems. An achromatic grating interferometer is used in our implementation of the processing approach. It is capable of producing and displaying in real time the real and imaginary parts of the Fourier transform of a 1-D incoherent optical input. Preliminary experimental results are presented to verify the theory and to demonstrate the processing approach.

II. Complex Degree of Spatial Coherence

Consider the system geometry illustrated in Fig. 1. The radiation emitted by a space-limited object field at the (α, β) plane is detected at far-field locations (x_1, y_1) and (x_2, y_2) . If the radiation is quasi-monochromatic and spatially incoherent, it can be shown that the complex degree of spatial coherence (CDSC) is equal to¹¹

The authors are with Environmental Research Institute of Michigan, Infrared & Optics Division, P.O. Box 8618, Ann Arbor, Michigan 48107.

Received 30 November 1983.

0003-6935/84/142282-10\$02.00/0.

© 1984 Optical Society of America.

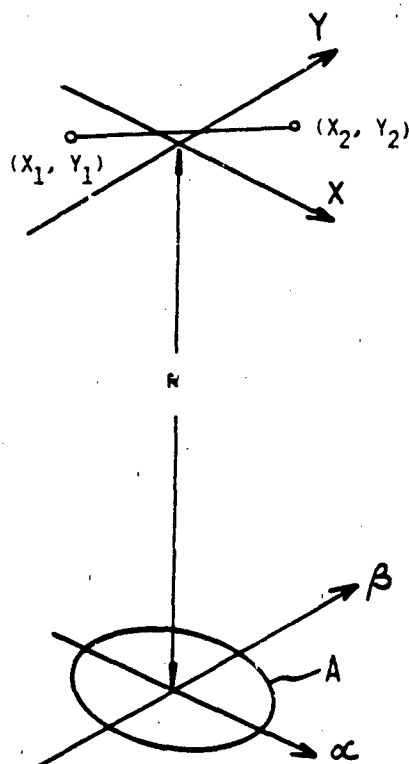


Fig. 1. System geometry relating the intensity distribution of an incoherent object field to the complex degree of spatial coherence at a detection plane in the far field.

$$C(u, v) = K \iint_A I(\alpha, \beta) \exp \left[\frac{-i2\pi}{\lambda} (u\alpha + v\beta) \right] d\alpha d\beta, \quad (1)$$

where

$$u = (x_1 - x_2)/R, \quad v = (y_1 - y_2)/R,$$

and K is a constant.

We see that there is a Fourier transform relationship between the input intensity distribution and the CDSC at far field. This relationship is sometimes known as the van Cittert-Zernike theorem. Thus, to obtain the Fourier transform of the intensity distribution of an incoherent input, one merely has to devise a means to measure the CDSC at far field. This can be achieved interferometrically by measuring the complex visibility of the interference fringes formed between the fields at (x_1, y_1) and (x_2, y_2) . The fringe visibility function is equal to

$$V[(x_1, y_1), (x_2, y_2)] = \frac{2\sqrt{I(x_1, y_1) I(x_2, y_2)}}{I(x_1, y_1) + I(x_2, y_2)} \cdot C[(x_1, y_1), (x_2, y_2)]. \quad (2)$$

For a homogeneous incoherent input, $I(x_1, y_1) = I(x_2, y_2)$, and the CDSC is space invariant in the far field. Thus we may write

$$V(u, v) = C(u, v). \quad (3)$$

With the Michelson stellar interferometer and other similar interferometric imaging systems, the spatial

frequencies are sampled by physically varying the separation of the detecting apertures. Such a sequential measurement scheme is too restrictive for use in a real-time processing system. The requirements that the input be quasi-monochromatic also makes the system very inefficient for inputs that are naturally polychromatic.

Roddier *et al.*¹² introduced a rotation shearing interferometer for astronomical imaging. Basically the input wave front is separated into two parts. One part is rotated 180° with a system of roof prisms or dove prisms and then recombined. At the center of the field which is the center of rotation there is no shear. Moving away from the center, increasing amounts of shear are introduced. Thus, unlike the Michelson stellar interferometer, all the spatial frequencies can be displayed at once. This technique is attractive for many applications, and it was suggested as an alternative to stellar speckle interferometry. However, similar to the Michelson stellar interferometer, it requires quasi-monochromaticity and is, therefore, rather inefficient in the processing of inputs that are spectrally wide band. George and Wang¹³ combined the rotation shearing interferometer with an achromatic transform optical system and demonstrated polychromatic cosine transform. Their system, however, requires a system of prisms to perform the rotation and a multielement optical system for the achromatic transformation. Moreover, switching from cosine to sine transformation cannot be easily achieved due to the difficulty in realizing achromatic $\pi/2$ phase shifts using reflective and refractive optics.

In this paper, we introduce a grating-based achromatic optical processor. It is capable of producing, in real time, cosine and sine transformations of inputs that are spatially and temporally incoherent. One major advantage offered by grating-based systems is simplicity. The grating interferometric processor tends to require much less hardware than conventional systems making it easier to fabricate and set up. The simplicity of the grating system also makes the processor more compact and vibration resistant.

III. Achromatic Grating Interferometer

The achromatic grating interferometer has been studied extensively and applied to many applications. Chang and Leith¹⁴⁻¹⁶ applied the interferometer to interferometric imaging and nondestructive testing. Leith and Roth^{17,18} studied the noise performance of the interferometer and the synthesis of the convolution integral for linear filtering. Collins¹⁹ demonstrated the construction of holograms and matched filters with incoherent light. Leith and Swanson²⁰ utilized the interferometer for the fabrication of noise-free diffractive optical elements. Tai and Aleksoff²¹ employed the grating interferometer arrangement in an imaging system for improved imaging through scattering media.

Leith and Chang,¹⁶ in particular, have recognized the ability of the grating interferometer to perform Fourier

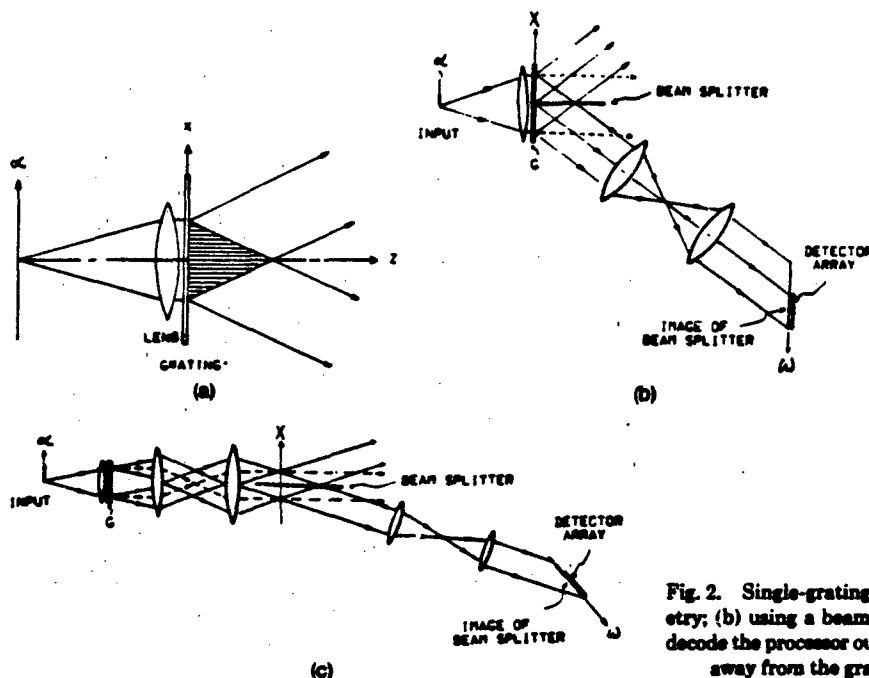


Fig. 2. Single-grating achromatic interferometer: (a) basic geometry; (b) using a beam splitter and a telescopic imaging system to decode the processor output; (c) imaging the fringe volume to a plane away from the grating to access the zero spatial frequency.

transformations. Their interest, however, was primarily in imaging where the image of an object was reconstructed by performing an optical transform with a coherent optical processor. To be able to utilize the interferometer as a processor, an appropriate decoding technique must be developed to produce a complex output that can be efficiently read out or interfaced to a computer.

The simplest achromatic grating interferometer that can be realized is composed of a single grating. Consider the optical arrangement depicted in Fig. 2(a). For a single point source located at $\alpha = \alpha_0$, the field amplitude in the volume where the ± 1 diffracted orders overlap is equal to

$$E(\alpha_0; x, z) = C\sqrt{S(\alpha_0)} \cdot \exp[i2\pi(P_0 - F)x + ikz\sqrt{1 - \lambda^2(P_0 - F)^2}] + \exp[i2\pi(P_0 + F)x + ikz\sqrt{1 - \lambda^2(P_0 + F)^2}]. \quad (4)$$

where $k = 2\pi/\lambda$, $S(\alpha_0)$ is the intensity of the point source, C is a constant, and $P_0 = \sin(\tan^{-1}\alpha_0/f)/\lambda$, f is the focal length of the lens, F is the spatial frequency of the grating, and λ is the wavelength of the source. The corresponding light intensity distribution in the fringe volume can be written as

$$I(\alpha_0; x, z) = |C|^2 S(\alpha_0) \left[1 + \cos \left[4\pi Fx + \frac{2\pi z}{\lambda} \cdot (\sqrt{1 - \lambda^2(P_0 + F)^2} - \sqrt{1 - \lambda^2(P_0 - F)^2}) \right] \right]. \quad (5)$$

Using a first-order approximation, the intensity distribution can be expressed as

$$I(\alpha_0; x, z) = |C|^2 S(\alpha_0) \left[1 + \cos \left[4\pi F \left(x - \frac{z\alpha_0}{f} \right) \right] \right]. \quad (6)$$

Now, if instead of having a single point source, we have

a spatially incoherent line source with intensity distribution $f(\alpha)$ extending from $\alpha = 0$ to $\alpha = l$, the output intensity distribution within a constant factor is

$$I(x, z) = \int_0^l f(\alpha) \left[1 + \cos 4\pi F \left(x - \frac{z\alpha}{f} \right) \right] d\alpha. \quad (7)$$

The intensity along the optical axis at $x = 0$ is

$$I(z) = \int_0^l f(\alpha) (1 + \cos \omega \alpha) d\alpha = \int_0^l f(\alpha) d\alpha + \int_0^l f(\alpha) \cos \omega \alpha d\alpha, \quad (8)$$

where $\omega = 4\pi Fz/f$.

The first term is simply a constant bias, and the second term we recognize as the cosine transform integral. Thus by reading out the intensity distribution along the optical axis, we obtain the bipolar cosine transform of the 1-D input intensity distribution plus a constant bias. We emphasize that the expression in Eq. (8) is not a function of wavelength. The transformation is performed achromatically.

The single-grating interferometer provides an extremely simple means of achieving optical transformation achromatically. However, the information is displayed as an intensity distribution along the optical axis, which is rather inaccessible. In particular, the zero spatial frequency is located at $z = 0$, right at the surface of the grating. One way to read out the intensity distribution along the z axis is to place a very thin beam splitter along the z - y plane at $x = 0$ as shown in Fig. 2(b). The intensity distribution can then be imaged to a convenient output plane to be measured. Unfortunately, it is not straightforward to place such a beam splitter right up against the grating. It nevertheless can be done using special optics. One may image the fringe volume directly with a telescopic imaging system as

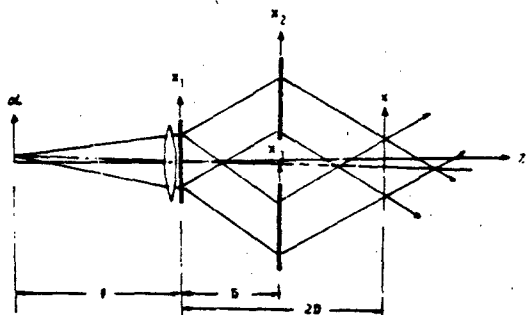


Fig. 3. Multiple-grating achromatic interferometer.

shown in Fig. 2(c) to make the fringe volume more accessible. However, the diffraction angles would be severely limited by the numerical apertures of the lenses. A better approach is to utilize a three-grating arrangement similar to that of Leith and Chang¹⁴ as shown in Fig. 3. The first grating G_1 has a spatial frequency of F , the second and third gratings are coplanar, and both have a spatial frequency of $2F$. The input light field is split into two first orders and the first grating and then recombined by the second and third gratings, G_2 and G_3 . A new fringe volume is formed about $z = 2D$, accessibly away from any grating. Moreover, spurious diffraction orders can now be easily removed to eliminate the spurious fringes and added bias that may otherwise be introduced. With a single point source located at $\alpha = \alpha_0$, the light field at the new fringe volume is equal to

$$E(\alpha_0, x, y) = C\sqrt{S(\alpha_0)} \cdot \exp[i2\pi(P_0 - F)x + ikD\sqrt{1 - \lambda^2(P_0 + F)^2} + ik(z + D)\sqrt{1 - \lambda^2(P_0 - F)^2}] \cdot \exp[i2\pi(P_0 + F)x + ikD\sqrt{1 - \lambda^2(P_0 - F)^2} + ik(z + D)\sqrt{1 - \lambda^2(P_0 + F)^2}]. \quad (9)$$

The corresponding light intensity distribution can be written as

$$I(x, z) = |C|^2 S(\alpha) (1 + \cos[4\pi Fx + kz(\sqrt{1 - \lambda^2(P_0 + F)^2} - \sqrt{1 - \lambda^2(P_0 - F)^2})]). \quad (10)$$

which can be approximated by

$$I(x, z) = |C|^2 S(\alpha) \left[1 + \cos \left[4\pi F \left(x - \frac{z\alpha}{f} \right) \right] \right]. \quad (11)$$

For a 1-D signal along the α axis ranging from 0 to l , the output intensity distribution becomes

$$I(x, z) = \int_0^l f(\alpha) \left[1 + \cos \left[4\pi F \left(x - \frac{z\alpha}{f} \right) \right] \right] d\alpha. \quad (12)$$

At $x = 0$, once again we have the cosine transform relationship

$$I(z) = \int_0^l f(\alpha) [1 + \cos(\omega\alpha)] d\alpha, \quad (13)$$

To perform a Fourier transformation, both real and imaginary output data are required. By simply translating the grating G_2 along the X_2 direction by one-fourth of a period (i.e., $\pi/2$ phase shift), the light intensity distribution along the z axis becomes

$$I(z) = \int_0^l f(\alpha) [1 + \sin(\omega\alpha)] d\alpha, \quad (14)$$

which is, of course, the sine transform of the input $f(\alpha)$. Thus both the real and imaginary parts of the complex transform output can be obtained. We may note that the shifting of the grating produces a $\pi/2$ phase shift for all wavelengths. The achromaticity of the system is maintained. This is in contrast to other interferometric systems using reflective or refracting optics.

Once again, the intensity distribution along the z axis can be read out by placing a thin beam splitter along the x - z plane as shown in Fig. 4. The intensity distribution along the beam splitter is mapped onto a convenient output plane outside the fringe volume using a one-to-one telescopic imaging system.

This simple implementation causes several problems. The beam splitter has to be very thin; a pellicle beam splitter might, therefore, be used. Pellicle beam splitters unfortunately have a tendency to vibrate. Although this is not a fundamental problem and can be solved using special optics, we decided to use an alternate arrangement for the demonstration.

The light distribution in the output fringe volume is equal to

$$I(x, y, z) = \int_0^l f(\alpha) \left[1 + \cos \left[4\pi F \left(x - \frac{z\alpha}{f} \right) \right] \right] d\alpha.$$

If we place a fourth grating with spatial frequency F at $z = z_0$ as shown in Fig. 5, the grating will demodulate the light back to zero spatial frequency, and the output light intensity becomes

$$I(z_0) = \int_0^l f(\alpha) \left[1 + \cos \left(\frac{4\pi F z_0 \alpha}{f} \right) \right] d\alpha, \quad (15)$$

which in effect gives the cosine transform of $f(\alpha)$ sampled at spatial frequency $4\pi F z_0 / f$. By translating the

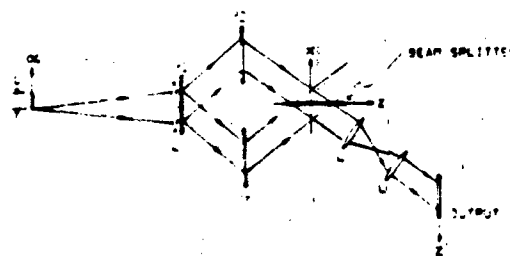


Fig. 4. Mapping the transform output in the fringe volume to a convenient output plane using a beam splitter.

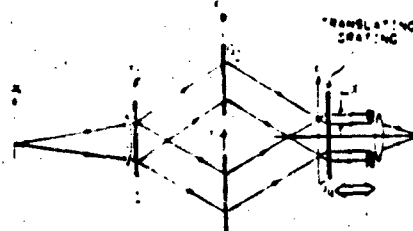


Fig. 5. Sampling of spatial frequencies with a translating fourth grating.

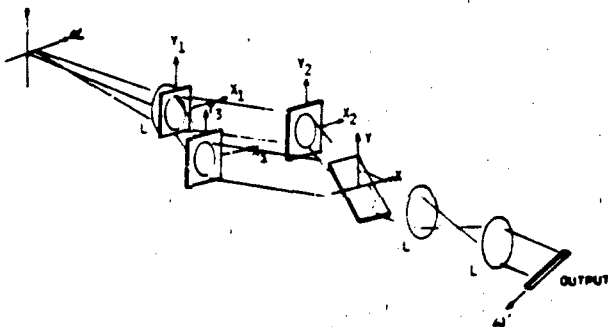


Fig. 6. Decoding the transform output with a tilted fourth grating.

fourth grating along the z axis over the entire fringe box, the cosine transform output can be scanned out. However, such a translation technique takes time, and our goal is real-time operation.

We note that Eq. (15) is not a function of x and y . The sampled cosine output can be obtained by measuring the intensity at any point of the output plane. If we tilt the fourth grating toward the x - z plane so that it traverses the fringe volume as illustrated in Fig. 6, different parts of the grating along the y direction will be sampling the intensity at different positions along the z direction. The output intensity distribution becomes

$$I(y) = \int_0^l f(\alpha) \left[1 + \cos \left(\frac{4\pi\alpha y F \tan\phi}{f} \right) \right] d\alpha, \quad (16)$$

which can be written as

$$I(\omega') = \int_0^l f(\alpha) d\alpha + \int_0^l f(\alpha) \cos(\omega'\alpha) d\alpha, \quad (17)$$

where

$$\omega' = (4\pi F y \tan\phi)/f,$$

and ϕ is the tilt angle of the fourth grating.

Once again, a biased output of the cosine transform is obtained. However, the spectrum is now displayed along the ω' direction, which is orthogonal to the α axis. The cosine spectrum, therefore, lies along a direction that is perpendicular to the 1-D input.

If we translate the fourth grating by one-eighth of a period (i.e., $\pm\pi/4$ phase shift), we obtain

$$I(\omega') = \int_0^l f(\alpha) d\alpha + \int_0^l f(\alpha) \sin(\omega'\alpha) d\alpha \quad (18)$$

or the sine transformation of $f(\alpha)$.

To perform complex Fourier transformations, we need both the real and imaginary parts. The cosine and sine transforms can be displayed simultaneously by using a split grating as the fourth grating at the output as shown in Fig. 7. The grating lines at the two halves of the grating are phase shifted by $\pi/4$. This produces a cosine transform at one side of the output and the sine transform at the other.

We note that the tilted grating decoding technique may also be applied to the single-grating interferometer by placing the tilted grating against the first grating

transversing the fringe volume. However, the presence of spurious diffraction orders may substantially degrade the transform output. In addition, transform information near dc may not be displayed due to blockage by the edge of the tilted grating.

When only cosine transforms are performed, the input must be either single sided (i.e., $0 \leq \alpha \leq l$) or an even function [i.e., $f(\alpha) = f(-\alpha)$] to avoid ambiguity. With a dual-channel system, however, the input is no longer limited to being single sided or even. The processor is actually performing the decomposition

$$\int_{-l}^l f(\alpha) \exp(-i\omega\alpha) d\alpha = \underbrace{\int_{-l}^l f(\alpha) \cos(\omega\alpha) d\alpha}_{\mathcal{F}_R} - i \underbrace{\int_{-l}^l f(\alpha) \sin(\omega\alpha) d\alpha}_{\mathcal{F}_I}$$

where $f(\alpha)$ is an arbitrary real and non-negative function, which in general is a combination of even and odd parts. That is, the decomposition is not in terms of the cosine transform of the even part and the sine transform of the odd part but rather in terms of \mathcal{F}_R and \mathcal{F}_I , which are the real and imaginary parts, respectively, of the Fourier transform. In this operating mode, the input can extend from $-l$ to l with unique information on both sides, and the space-bandwidth product of the processor is in effect doubled. This doubling of the space-bandwidth product can be considered to occur because the system acts as a dual-channel processor simultaneously performing the real and imaginary parts of the Fourier transformation. A more detailed discussion on the space-bandwidth product of the grating interferometric processor is given in a later section.

IV. Experimental Results

An interferometric optical processor was set up using the configuration illustrated in Fig. 6. As the input, a ground glass diffuser was backilluminated by an unfiltered xenon arc lamp to produce an incoherent light source, which in turn was used to illuminate a slit and transparency. To test if the system can produce the correct Fourier transform output, a transparency with an intensity transmittance of $1 + \cos(2\pi g\alpha)$ was used. Thus the input is given by $f(\alpha) = \text{rect}[(\alpha - \alpha_0)L][1 + \cos(2\pi g\alpha)]$. The cosine/sine transform outputs were read out using a 1024-element linear detector array. In Fig. 8(a), we show the cosine transform output obtained with the interferometric processor. For comparison, we computed the Fourier transform of a function:

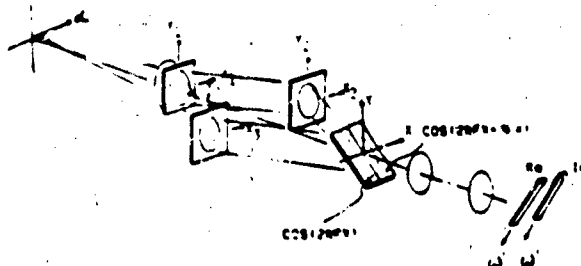


Fig. 7. Simultaneous cosine and sine transformations.

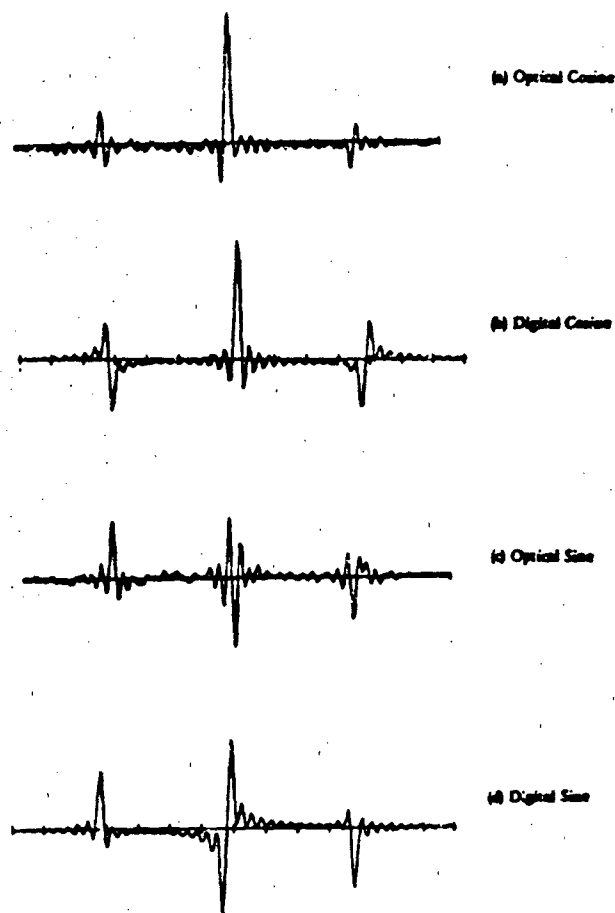


Fig. 8. Optically generated cosine and sine transforms vs the digitally computed versions.

$$f(\alpha) = W(\alpha) \text{rect}\left(\frac{\alpha - \alpha_0}{L}\right) [1 + \cos(2\pi g(\alpha + \phi))] \exp(i\theta), \quad (19)$$

where $\text{rect}[(\alpha - \alpha_0)/L] = 1$ for $\alpha_0 - L/2 \leq \alpha \leq \alpha_0 + L/2$, $W(\alpha)$ is an apodizing factor added to account for the nonuniform illumination of the input, α_0 is the offset of the input from the axis, g is the spatial frequency, ϕ is the phase of the input cosine function, and θ is an arbitrary phase.

The choice of the grating position that is designated as cosine or sine transform is arbitrary and unimportant as long as an exact $\pi/2$ phase shift is introduced between the sine and cosine transforms and a consistency is maintained. The difference in the outputs caused by different initial choices of the grating position is simply a constant phase. (A similar situation arises in coherent optical processing where a coherent reference beam is introduced to measure the complex output of the optical processor.) In our experiment, the constant phase term $\exp(i\theta)$ was obtained by varying θ in the computation until the real part of the zero order of the digital Fourier transform matched that of the optical output. In Fig. 8(b), we show the computed real part of the Fourier transform. Except for a small phase difference, there is a very good correspondence between the optically

obtained and digitally computed results. The small phase error might have been caused by irregularity in the local frequency of the gratings.

The fourth grating was then translated by one-eighth of a period to produce a $\pi/4$ phase shift on the recombined beams. The optically obtained sine transform output is shown in Fig. 8(c). For comparison, the corresponding computed imaginary part of the Fourier transform is shown in Fig. 8(d). Once again, the optical output matches the digitally computed result.

V. Comparison to a Michelson Stellar Interferometer

The operation of this system can be explained more intuitively by going back to the Michelson stellar interferometer. The Michelson stellar interferometer in its basic form is simply two apertures separated by a distance d as shown in Fig. 9(a). The CDSC is obtained by measuring the complex visibility of the fringes formed for different separations of the apertures. We see from Fig. 9(b) that we have a similar situation with the grating interferometer. The interfering light fields are sheared by an amount $\Delta x = z' \tan[\sin^{-1}(\lambda F)]$, where F is the spatial frequency of the grating. Thus, similar to the Michelson stellar interferometer, two parts of a wave front separated by a transverse distance Δx are made to interfere, and the resulting fringe visibility along the z axis, therefore, follows a Fourier transform relationship with the source intensity distribution. Unlike the Michelson interferometer where the visibility for each value of Δx must be measured separately, the grating interferometer presents the interference fringes for the different shear distances simultaneously at different positions of z . This interferometric optical

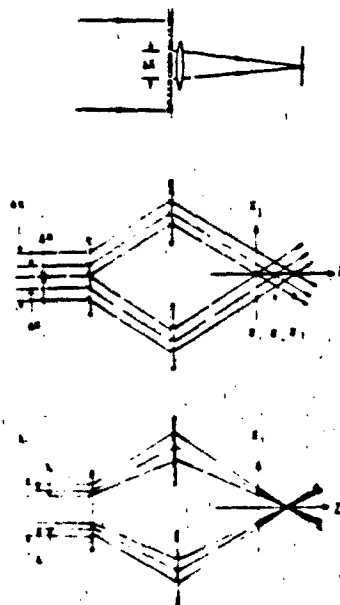


Fig. 9. Comparison with a Michelson-Stellar interferometer: (a) Michelson stellar interferometer; (b) simultaneous display of all spatial frequencies with the grating interferometer; (c) wavelength-dependent shearing of input wave front.

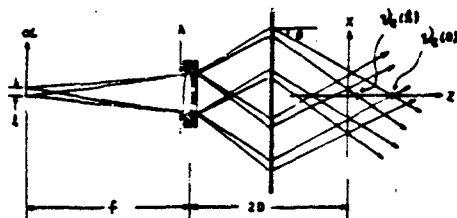


Fig. 10. Shifting of fringe volume for off-axis input point.

processor is, therefore, basically an interferometer that is capable of measuring in parallel the 1-D CDSC of a field emanated from a homogeneous incoherent line source at far field as created by the collimating lens.

The spatial frequency as measured by a Michelson interferometer is given by $u = 2\pi\Delta x/\lambda f$, which is wavelength dependent. A Michelson interferometer can, therefore, operate only with quasi-monochromatic radiation. To make the system achromatic, a variable amount of shear must be introduced so that $\Delta x(\lambda)/\lambda = \text{constant}$. The amount of shear introduced by the grating interferometer varies with wavelength, since to the first order, $\Delta x = 2F\lambda z$, as illustrated in Fig. 9(c). The spatial frequency is thus $u = 4\pi Fz/f$, which is wavelength independent and hence achromatic.

VI. Comparison to Coherent Optical Processing

Although the interferometric processor operates on incoherent inputs, its performance characteristics are very similar to a coherent optical processor. For a coherent system, the transform relationship can be written as

$$F(p) = \int_{-\infty}^{\infty} f(\alpha) \exp\left(\frac{i2\pi\alpha p}{\lambda f}\right) d\alpha, \quad (20)$$

and for the interferometric optical processor,

$$F_R(z) = \int_{-\infty}^{\infty} f(\alpha) \cos\left(\frac{4\pi Fz\alpha}{f}\right) d\alpha \quad (21)$$

and

$$F_I(z) = \int_{-\infty}^{\infty} f(\alpha) \sin\left(\frac{4\pi Fz\alpha}{f}\right) d\alpha. \quad (22)$$

The difference between the two processors is in the scaling factors $2\pi/\lambda f$ and $4\pi F/f$. The scaling factor for a coherent optical processor is inversely proportional to wavelength, while the scaling factor for the interferometric processor is independent of wavelength. Hence the interferometric processor is equivalent to an achromatic Fourier transform system.^{2,3}

For systems that use AO modulators or discrete sources (e.g., the vector-matrix multiplier) as input devices, the space-bandwidth product is typically input device limited and can be easily defined. For a coherent optical processor and an interferometric optical processor, on the other hand, the space-bandwidth product is usually processor-limited and is dependent on many factors such as the exact optical configuration, the $f/\text{No.}$ of the transform or collimating lens, the aperture of the lens, and the performance of the lens. In the following,

we compute the space-bandwidth product (SBWP) of the single-grating and the multiple-grating interferometers. The approximations and assumptions used in the computation are listed:

(1) The angular bandwidth of the gratings in the processor are very wide (e.g., surface relief gratings).

(2) The spurious diffraction orders are not a problem, and no stops are used in the system. (This assumption is always valid for systems that utilize beam splitters to demodulate the output. It is also valid for the multiple-grating system using a tilted fourth grating for output demodulated if the gratings are properly fabricated. The effects of spurious diffraction orders will be discussed in a later section.)

(3) The gratings are of sufficient size that the entire field over the full angular bandwidth is diffracted by the gratings.

(4) The field distribution along the optical z axis is considered as the output plane. [In actual system operation, it is necessary to transfer this output plane to a more accessible plane using a beam splitter or a grating. This analysis is directly applicable to a system that utilizes a beam splitter to demodulate the output (Fig. 4). With the use of a tilted fourth grating, however, the performance characteristic may be degraded in the decoding process, and the system SBWP may be lower than computed.]

(5) First-order approximations are used to describe the operation of the interferometer.

For both the single- and multiple-grating interferometric systems, except for the change in coordinate position, we have

$$I(z) = \int_{-1}^1 f(\alpha) d\alpha + \int_{-1}^1 f(\alpha) \cos(\omega\alpha) d\alpha,$$

where $\omega = 4\pi Fz/f$.

Consider specifically the multiple-grating processor as illustrated in Fig. 10. The fringe box translates down or up depending on the position of the input point. For a point input at $\alpha = \alpha_0$, the fringe box extends along the z axis up to

$$z' = \left(\frac{A}{2} - \frac{2D\alpha_0}{f}\right) / T,$$

where

$$T = \tan\left(\sin^{-1}\left[\lambda F - \sin\left[\tan^{-1}\left(\frac{\alpha_0}{f}\right)\right]\right]\right) \quad (23)$$

corresponding to a cutoff spatial frequency of

$$\nu_c(\alpha_0) = \frac{2F}{fT} \left(\frac{A}{2} - \frac{2D\alpha_0}{f}\right). \quad (24)$$

For the on-axis point $\alpha_0 = 0$, the cutoff frequency is a maximum and is given by

$$\nu_c(0) = \frac{A \cos\theta}{\lambda f}, \quad (25)$$

where

$$\theta = \sin^{-1}(F\lambda) \quad (26)$$

is the diffraction angle shown in Fig. 10. Notice that the cutoff frequency is wavelength dependent. We also

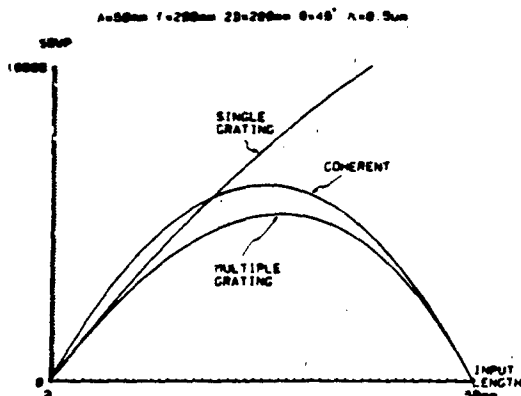


Fig. 11. Space-bandwidth products of a single-grating interferometric processor, a multiple-grating interferometric processor, and a coherent optical processor.

point out that, except for the cosine factor, Eq. (25) describes the highest frequency that can be coherently processed by a Fourier transform lens with aperture width A , focal length f , and the input placed a focal length in front of the lens. In fact, an expression equivalent to that of Eq. (24) for such a coherent processor is given in the Appendix.

Now consider an input signal of length $2l$, extending from $\alpha = -l$ to $\alpha = l$. The end point l establishes a cutoff frequency $\nu_c(l)$. Although one could define a space-bandwidth product (SBWP) given by the product of the line length by the maximum cutoff, i.e., $4l\nu_c(0)$, it is more meaningful for arbitrary inputs to establish the SBWP only as specified over the uniform (nontapering) part of the spectrum as given by the lowest cutoff frequency $\nu_c(l)$. Thus we define the SBWP as

$$\text{SBWP}(l) = 4l\nu_c(l), \quad (27)$$

which with substitution from Eq. (24) becomes

$$\text{SBWP}(l) = \frac{2l}{f} \left(\frac{A}{2} - \frac{2Dl}{f} \right). \quad (28)$$

Equations (24)–(28) also hold for the single-grating interferometer by letting $D = 0$. The single-grating interferometer can be considered to be the limit of the multiple-grating interferometer as D approaches zero. It is seen from Eq. (28) that the SBWP is maximized for $D = 0$, i.e., for the single-grating interferometer.

It is worthwhile to compare the above results with those for a classical Fourier transform lens used as a coherent optical processor (see Appendix). The SBWP, defined in a similar way as for Eq. (28), for the coherent processor is

$$\text{coh}[\text{SBWP}(2l)] = 2l/\lambda \cdot (\sin[\tan^{-1}[(A - 2l)/f]]). \quad (29)$$

where the input extends from $-A/2$ to $2l - A/2$.

In Fig. 11, the SBWP is plotted as a function of the length of the input for the coherent optical processor and for the two-grating interferometer geometries. Note that for the multiple-grating interferometer and the coherent optical processor, there is an optimum

input length. To maximize further the SBWP of the multiple-grating interferometer, it is necessary to minimize the length of the interferometer $2D$. (This is equivalent to moving the input closer to the Fourier transform lens in the case of a coherent optical processor.) As we shorten the interferometer, the gratings eventually collapse onto a single plane, and we essentially have the single-grating interferometer. (This is similar to putting the input right in front of the transform lens of the coherent optical processor.)

The above space-bandwidth product is computed from geometric considerations. A second factor that can limit the space-bandwidth product of the system is the dynamic range of the output detector array. The bias level is determined by the integrated input signal level

$$B = \int_{-l}^l f(\alpha) d\alpha.$$

As l increases so does the bias level. Thus the number of input points that can be processed for the worst case is equal to the dynamic range of the output detector. The space-bandwidth product, however, can be much larger if the transform of the input consists of only a small number of points (e.g., a sinusoidal input). In that case, the space-bandwidth product of the system is limited by the system geometry.

We should note that the same dynamic range limitation also applies to a coherent optical processor if the complex output is to be read out with a detector array. However, there is more flexibility with the coherent system. For example, if the input data are on a carrier and the information around dc is unimportant, the reference beam can be lowered to a level corresponding to the highest signal level in the desired portion of the output spectrum. With the interferometric processor, on the other hand, the bias is fixed at a level corresponding to the dc output.

We emphasize that unlike many other optical systems that utilize gratings (e.g., the achromatic Fourier transform system), spurious diffraction orders do not necessarily pose a problem for the grating interferometric processor. With the use of a beam splitter to decode the output, the spurious orders have minimal effect, since they propagate in directions away from the output plane as long as the angular subtend of the input is less than the diffraction angle of the grating. This is true for both the single-grating and multiple-grating arrangements utilizing beam splitters. For a multiple-grating system that employs a tilted grating to demodulate the output, the spurious diffraction orders are also not a serious problem. First, the higher diffraction orders propagate away from the output plane, and for the right arrangement they will not pose a problem. The zero order does propagate toward the output plane, but it can be suppressed significantly. For example, if a thin sinusoidal phase grating is used, the powers in the various diffraction orders follow the Bessel functions. By adjusting the exposure in the fabrication of the grating to where the zeroth-order Bessel function goes to zero, the dc term can be substantially suppressed.

Furthermore, the zeroth order is incoherent with the first orders that are being combined (large path differences). Thus the effect of the dc term that remains is to add a small uniform bias to the output. Spurious orders, however, do create serious problems when using a tilted grating to decode the output of a single grating system, and such an arrangement is generally not desirable.

VII. Applications

The interferometric optical processor can be configured to perform operations currently accomplished by other optical processors. In addition, it can perform operations that cannot be easily done otherwise, since it operates on incoherent light.

For example, to process a temporal signal, the scanning electron beam of a CRT can be used to convert the temporal electrical signal into a spatial formatted light signal. The processed output is received by a detector array which is read out after integrating over the time of a complete scan of the electron beam. Such a system can operate over a large range of frequencies by varying the scan rate of the electron beam. The ease in obtaining the real and imaginary parts of the complex Fourier transform output gives the interferometric processor a potential advantage over optical systems using AO modulators and SAW devices.

The interferometer is a parallel processing device, and its capability is not fully utilized when used to process single-channel temporal signals. For applications where parallel inputs are available (e.g., from an antenna array), the inputs can be used to drive individual LEDs in a linear array. Together with an array of individually addressable detectors, the system can be used to perform n -point discrete Fourier transforms at a rate determined by the frequency response limit of the LEDs. As compared to the vector-matrix multiplier, the interferometric processor has the advantage of simplicity requiring only simple gratings and collimation optics instead of complicated 2-D masks and beam-forming optics.

More important, however, is the ability of the interferometric optical processor to operate on completely incoherent inputs. The system, therefore, has the potential to perform Fourier transformations on signals directly from the real world using light emanating from the object scene itself.

VIII. Summary

We have introduced an optical processor which is capable of performing complex spatial 1-D Fourier transforms on incoherent optical inputs. One possible implementation of the processing approach using a grating interferometer was presented, and the operation of an interferometric optical processor is experimentally demonstrated. The potential ability of the system to directly process images using the light emanated from an object scene removes limitations imposed by input devices and opens new avenues for optical processing. The research on this type of interferometric processor is still in its initial stages, and much has yet to be developed.

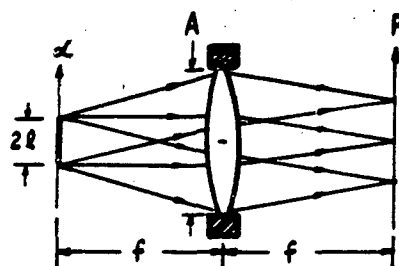


Fig. 12. Geometry of a coherent optical processor for the processing of real inputs.

oped. The optical configurations presented are only examples of many other possible implementations of the interferometric optical processor. Alternative system configurations with different performance characteristics that are optimized for specific applications can be developed.

The work was supported by the U.S. Army Research Office. Parts of this paper were presented at the International Optical Computing Conference, Apr. 1983.²²

Appendix: Space-Bandwidth Product of a Coherent Optical Processor

For an optical Fourier transform lens to process the input signal without loss of information, all the light emanating from the input aperture must be passed by the lens aperture, i.e., no vignetting. Consider the 1-D optical processor illustrated in Fig. 12. At position α the cutoff frequency defined by geometry considerations is given by

$$\nu_c(\alpha) = \lambda^{-1} \sin[\tan^{-1}\{(A - 2|\alpha|)/2f\}]. \quad (A1)$$

Thus the cutoff frequency varies along the input aperture. It is possible to define a maximum space-bandwidth product via

$$\text{SBWP}_{\max} = 4\nu_c(0), \quad (A2)$$

where the input is assumed to extend from $-l$ to $+l$ and the extra 2 comes from the two sidebands. However, to insure that the input is processed without loss of information, the highest spatial frequency of the input must be limited to $\nu_c(l)$. Then the SBWP becomes

$$\text{SBWP}(l) = 4\nu_c(l). \quad (A3)$$

If the input is real, the transform is Hermitian. One sideband of the output spectrum can be discarded without loss of information. By placing the input asymmetrically from $-A/2$ to $A/2$, the (one-sided) cutoff frequency becomes

$$\nu_c(2l) = \sin[\tan^{-1}\{(A - 2l)/f\}]. \quad (A4)$$

where $0 < l < A/2$. The SBWP becomes

$$\text{SBWP}(l) = 2\nu_c(2l). \quad (A5)$$

To determine the optimum input size for a given value of A and f , we let $2l = nA$ and take the partial derivative of Eq. (A3) to get

$$\frac{(2n-1)}{(1-n)^3} = \frac{A^2}{4f^2} \quad (\text{A6})$$

and of Eq. (A5) to get

$$\frac{(2n-1)}{(1-n)^3} = \frac{A^2}{f^2} \quad (\text{A7})$$

For lenses with $f/\text{Nos.}$ of $f/2$ or slower, n is nearly 0.5 for both cases. That is, the optimum SBWP tends to be obtained when the input aperture size is one-half of the lens aperture size.

References

1. J. W. Goodman, *Introduction to Fourier Optics* (McGraw-Hill, New York, 1968); F. T. S. Yu, *Introduction to Diffraction, Information Processing, and Holography* (MIT Press, Cambridge, 1973).
2. R. H. Katyl, "Compensating Optical Systems. 3: Achromatic Fourier Transformation," *Appl. Opt.* 11, 1255 (1972).
3. G. M. Morris and N. George, "Frequency-Plane Filtering with an Achromatic Optical Transform," *Opt. Lett.* 5, 446 (1980).
4. D. Das and F. M. M. Ayuo, in *Applications of Optical Fourier Transforms*, H. Stark, Ed. (Academic, New York, 1982), Chap. 7.
5. N. J. Berg, J. N. Lee, M. W. Caseday, and B. J. Udelson, "Surface Wave Delay Line Acoustooptic Devices for Signal Processing," *Appl. Opt.* 18, 2767 (1979).
6. A. W. Lohmann and W. T. Rhodes, "Two-Pupil Synthesis of Optical Transfer Functions," *Appl. Opt.* 17, 1141 (1978).
7. W. Stoner, "Incoherent Optical Processing via Spatially Offset Pupil Masks," *Appl. Opt.* 17, 2454 (1978).
8. G. L. Rogers, *Noncoherent Optical Processing* (Wiley, New York, 1968).
9. M. A. Monahan, K. Bromley, and R. P. Brocker, *Proc. IEEE* 65, 121 (1977).
10. J. W. Goodman, A. R. Dias, and L. H. Woody, "Fully Parallel High-Speed Incoherent Optical Method for Performing Discrete Fourier Transforms," *Opt. Lett.* 2, 1 (1978).
11. M. Born and E. Wolf, *Principles of Optics* (Pergamon, New York, 1975).
12. F. Roddier, C. Roddier, and J. Demarcq, *J. Opt. (Paris)* 9, 145 (1978).
13. N. George and S. Wang, "Cosinusoidal Transforms in White Light," *Appl. Opt.* 23, 787 (1984).
14. B. J. Chang, Ph.D. Thesis, U. Michigan, Ann Arbor (1974).
15. B. J. Chang and E. N. Leith, "Space-Invariant Multiple-Grating Interferometers in Holography," *J. Opt. Soc. Am.* 69, 689 (1979).
16. E. N. Leith and B. J. Chang, "Image Formation with Achromatic Interferometer," *Opt. Commun.* 23, 217 (1979).
17. E. N. Leith and J. A. Roth, "White Light Optical Processing and Holography," *Appl. Opt.* 16, 2565 (1977).
18. E. N. Leith and J. A. Roth, "Noise Performance of an Achromatic Coherent Optical System," *Appl. Opt.* 18, 2803 (1979).
19. G. D. Collins, "Achromatic Fourier Transform Holography," *Appl. Opt.* 20, 3109 (1981).
20. E. N. Leith and G. J. Swanson, "Recording of Phase-Amplitude Images," *Appl. Opt.* 20, 3081 (1981).
21. A. Tai, C. C. Aleksoff, and B. J. Chang, "Imaging Through Scattering Media by Interferometric Techniques," *Appl. Opt.* 20, 2484 (1981).
22. A. Tai and C. C. Aleksoff, "An Incoherent Optical Processor for Real Time Complex Fourier Transformation," *Proc. Soc. Photo-Opt. Instrum. Eng.* 422, 99 (1983).

APPENDIX G

ADDITIONAL REQUESTED INFORMATION

The following people were supported in part by this contract:

Dr. C. C. Aleksoff
Dr. T. M. Stachelek
Dr. A. M. Tai
Dr. L. M. Peterson
Mrs. R. Roumaya

ERIM is not an educational institute and no degrees were awarded for people supported under this contract.

The publications submitted or published under at least partial ARO support are:

C. C. Aleksoff, "Synthetic Aperture Technique at Near-Millimeter Wavelengths," SPIE, Vol. 259, 1980, pp. 115-124

C. C. Aleksoff and L. M. Peterson, "Bandwidth Compression Using a Mode-Locked Local Oscillator," Proc. SPIE, Vol. 380, 1983, pp. 239-247

C. C. Aleksoff and L. M. Peterson, "Laser Heterodyne Ranging Using a Mode-Locked Local Oscillator for Bandwidth Compression," submitted to Optical Engineering.

C. C. Aleksoff and T. M. Stachelek, "Tapped-Fiber Spectrum Analyzer," to be submitted to Optics Communications.

C. C. Aleksoff, I. J. LaHaie, and A. M. Tai, "Optical-Hybrid Back-projection Processing," Proc. SPIE, Vol. 422, 1983, pp. 89-95.

A. M. Tai and C. C. Aleksoff, "An Incoherent Optical Processor in Real-Time Complex Fourier Transformation," Proc. SPIE, Vol. 422, 1983, pp. 99-104.

A. M. Tai and C. C. Aleksoff, "Grating-Based Interferometric Processor for Real-Time Optical Fourier Transformation," Applied Optics, 23, 15 July 1984, pp. 2282-2291.

END

FILMED

8-85

DTIC